Equilibrium fluid-crystal interfacial free energy of bcc-crystallizing aqueous suspensions of polydisperse charged spheres

Thomas Palberg,[1,*] Patrick Wette,[2,3] and Dieter M. Herlach[2]
[1]*Institut für Physik, Johannes Gutenberg Universität Mainz, 55099 Mainz, Germany*
[2]*Institut für Materialphysik im Weltraum, Deutsches Zentrum für Luft- und Raumfahrt (DLR), 51147 Köln, Germany*
[3]*Space Administration, Deutsches Zentrum für Luft- und Raumfahrt (DLR), 53227 Bonn, Germany*
(Received 13 June 2015; revised manuscript received 15 November 2015; published 3 February 2016)

The interfacial free energy is a central quantity in crystallization from the metastable melt. In suspensions of charged colloidal spheres, nucleation and growth kinetics can be accurately measured from optical experiments. In previous work, from these data effective nonequilibrium values for the interfacial free energy between the emerging bcc nuclei and the adjacent melt in dependence on the chemical potential difference between melt phase and crystal phase were derived using classical nucleation theory (CNT). A strictly linear increase of the interfacial free energy was observed as a function of increased metastability. Here, we further analyze these data for five aqueous suspensions of charged spheres and one binary mixture. We utilize a simple extrapolation scheme and interpret our findings in view of Turnbull's empirical rule. This enables us to present the first systematic experimental estimates for a reduced interfacial free energy, $\sigma_{0,bcc}$, between the bcc-crystal phase and the coexisting equilibrium fluid. Values obtained for $\sigma_{0,bcc}$ are on the order of a few k_BT. Their values are not correlated to any of the electrostatic interaction parameters but rather show a systematic decrease with increasing size polydispersity and a lower value for the mixture as compared to the pure components. At the same time, σ_0 also shows an approximately linear correlation to the entropy of freezing. The equilibrium interfacial free energy of strictly monodisperse charged spheres may therefore be still greater.

DOI: 10.1103/PhysRevE.93.022601

I. INTRODUCTION

Like their atomic counterparts, colloidal clusters bridge between the realms of individual particles and of macroscopic bulk phases. New scale related features appear in their structural and dynamic properties and challenge their definition and description by well known purely macroscopic, colloidal, or quantum concepts. Recently in this intensively studied field, much progress has been made by combining complementary approaches like analytical theory and simulations or microscopy and scattering experiments. At the same time, well controlled model systems became available. Their tuneable interactions are in many cases accurately described by analytical expressions. Because of this, we are now aware of a large variety of different colloidal cluster types with different shape, internal structure, dynamics, and cluster-cluster interaction. Their formation, stability and properties are of fundamental interest [1–7] but moreover play a decisive role in practical processes, like gelation, coating, or food processing [8,9]. Clusters also appear as embedded ensembles in colloidal (shear) melts during the initial steps of freezing [10,11] and vitrification [12]. Unlike in condensation problems, here the differences between cluster and melt properties (e.g., density or structure) may become very small and require special care in cluster discrimination [13–15]. Moreover, cluster and interfacial structure may be time and/or size dependent [16–19]. Cluster energetics, dynamics, and growth kinetics determine the polymorph selection and the emerging solid's microstructure [16,20,21] but furthermore may make them a crystallization frustrating agent in vitrifying melts [12,22–24]. In this instance, their local orientation prevents coalescence and their local symmetry hinders a global transformation to the crystalline state [25,26]. Clusters are therefore considered to be an important transient state in the formation of (colloidal) solids. Both simulations and microscopy reveal the shape of such nuclei to be anisometric and their surface to be rough, extended, and (as expected by scale arguments) not well definable in terms of continuous, differentiable two dimensional manifolds [16,17,20,27,28]. Light scattering [10,24,29–32] and small angle x-ray scattering experiments [33] return the statistically well founded temporal development of the orientationally averaged cluster sizes, the cluster numbers, and their rate of production [34–36]. Given their accessibility by complementary methods working on different length scales, colloidal clusters appear to be well-suited models for detailed studies of phase transformation processes as well as critical assessments of the concepts employed in their description.

The key quantity of interest in the present paper is the reversible work involved in the creation of a dividing surface, an interface between a cluster and its surroundings. It is termed surface tension, interfacial tension, or interfacial free energy (IFE). On the macroscopic level with adjacent continuous phases, this is a well-defined quantity and it can be determined with high accuracy by theoretical, numerical, and experimental techniques. On the level of clusters, a statistically meaningful description can only be based on orientationally averaged quantities. To connect these data to the desired (equilibrium) thermodynamic quantities, no generally accepted scale bridging theory is available. Thus very often approximate and empirical schemes are used to parametrize the raw data. A widely used parametrization for crystallization processes is the so-called classical nucleation theory (CNT) [37–42]. Since it basically ignores the cluster nature of nuclei and takes a macroscopic view of this microscopic problem, conceptual

*Corresponding author: palberg@uni-mainz.de

difficulties have been pointed out. (The interested reader is referred to Appendix A, where one finds a short outline of the main objections raised and some suggestions to circumvent these.) Still this approach has turned out to be eminently practical and versatile. It has also opened a way to obtain estimates of CNT-based effective IFEs from nonequilibrium crystallization experiments on systems as diverse as metals and colloids, hard spheres (HSs), and Lennard-Jones particles. CNT therefore became central in modeling the kinetics of first order phase transitions [43–46]. In polymorph selection, for instance, CNT-based kinetic arguments suggest that the cluster with the lowest nucleation barrier will reach its critical size and continue to grow [47,48], rather than that of the lowest free energy. CNT also found important practical application, e.g., in the fabrication of advanced soft materials [49–51]. Moreover, intriguingly simple empirical rules have been discovered applying CNT to crystallization phenomena. This paper takes particular interest in Turnbull's rule relating the IFE per particle in a surface to the latent heat of fusion per particle [52] or the entropy of fusion per particle [53] in a linear fashion.

In fact, it is with this rule in mind that in the present paper we undertake a comprehensive analysis of presently available CNT-based estimates of effective nonequilibrium IFEs for several systems of polydisperse charged sphere suspensions. The original data were obtained by optical experiments [11,30,31,54–56] yielding nucleation rate densities via KJMA theory [57–59] or Kashchiev's theory of transient nucleation [60]. Nucleation rate densities in turn were parametrized using CNT [11,55] with the independently measured melt metastability expressed in terms of the chemical potential difference between the two phases, $\Delta\mu$, as input [61,62]. This yielded kinetic prefactors and the CNT-based effective nonequilibrium IFEs, γ, used as the starting point of the present analysis.

In our analysis, we go beyond previous work, as we apply a simple extrapolation scheme to obtain estimates of CNT-based effective equilibrium IFEs for bcc-crystallizing model systems. We compare these to values for equilibrium IFEs obtained for various systems by direct observation of equilibrated macroscopic interfaces. We also compare to nonequilibrium IFEs, both CNT-based effective IFEs for atomic and molecular systems and more directly obtained ones from, e.g., direct observations of cluster fluctuations. Our comparison to these data from both experiments and simulations reveals that the IFEs of polydisperse charged colloidal systems range between those of metals and of monodisperse hard spheres but are much larger than those found for point Yukawa systems. Next we search for correlations of the inferred CNT-based effective equilibrium IFEs with the system specific parameters characterizing strength and range of the prevailing electrostatic interactions as well as to other properties of the cluster constituents, e.g., their colloid specific polydispersity. Interestingly we observe no correlations to the former quantities. However, we do observe a pronounced anticorrelation of the IFE to the system polydispersity. We further propose an extension of the extrapolation scheme based on Turnbull's relation, some elementary thermodynamics, and the assumption that the entropy of freezing does not depend on the degree of metastability. This procedure returns estimates of other thermodynamic quantities like the entropy of freezing, the latent heat of freezing, and Turnbull's coefficient. Our findings allow rationalization of the observed anticorrelation of the IFEs to the system polydispersity in terms of the entropy differences between the adjacent structures. They further support entropy based theoretical arguments for the dependence of Turnbull's coefficient on crystal structure.

Data for comparison come from different experimental and theoretical approaches on a large variety of systems. Absolute values of the IFE differ by orders of magnitude due to the different particle number densities, n, involved for, e.g., metals ($n \approx 10^{26}$ m^{-3}) and colloids ($n \approx (10^{17}$–$10^{19})$ m^{-3}). In view of this, we follow the original work of Turnbull [52] and normalize γ with the area taken by a single particle in the interface, A_P, to compare reduced values of the interfacial free energy, $\sigma = \gamma A_P$. In the literature, different measures for A_P have been employed. For metals [52] and hard spheres (HSs) [29,63,64], but sometimes also for strongly screened charged spheres [65], A_P was approximated by $(2a)^2$, where a is the particle radius. This is generally considered as a physically reasonable approximation, since at the large volume fractions encountered in close-packed metals, HSs, and slightly charged HS crystals the particles are (nearly) in contact. Further, any change in density with increased metastability is generally small, such that $A_P \cong$ const for all T below the melting temperature T_M, respectively all volume fractions above the freezing volume fraction ($\Phi_{F,HS} = 0.492$ [66]). By contrast, in low salt charged sphere (CS) crystals the nearest neighbor distance at melting is usually on the order of several particle diameters due to mutual electrostatic repulsion ($\Phi_F \leqslant 0.01$ [67]; see also Table I). Here, the area of interest is the square of the nearest neighbor distance, ${d_{NN}}^2$. Note that this area will shrink considerably when the particle number density is increased above the melting density. For the here-analyzed samples the spread in ${d_{NN}}^2$ covers about three orders of magnitude between its value at melting for PnBAPS70 ($n_{M,PnBAPS70} = 2\ \mu$m^{-3}) and the one at the largest investigated particle concentration for Si77 ($n_{\max,Si77} = 80\ \mu$m^{-3}). We therefore normalize each nonequilibrium IFE by the square of the nearest neighbor distances at the particle number density investigated, ${d_{NN}}^2 = n^{-2/3}$. We further use $k_B T_M$ as the energy unit for the reduced IFEs, where T_M denotes the melting temperature.

Important reference data for our comparison come from studies of equilibrated interfaces. Here, previous studies focused on systems where the melt is in contact with a close-packed crystal structure. Equilibrium IFEs, stiffness, and anisotropy have been studied for theoretical model systems like hard spheres (HSs) [64,66,68–73], Lennard-Jones (LJ) particles, or particles interacting via inverse power potentials [68,74–77]. These quantities have also been studied in simulations of various metal systems utilizing embedded atom potentials [78,79]. Experimental equilibrium studies are rare for metal systems due to the practical difficulties involved in working at the melting point [45,80]. Equilibrated interfaces have, however, been studied experimentally in HS colloidal systems [81]. Hernández-Guzmán and Weeks, for instance, performed a capillary wave analysis of the equilibrated interface between a face centered cubic (fcc) crystal of HS and the adjacent HS fluid [82]. Rogers and Ackerson measured the IFE for HS crystals from a careful groove analysis of a

TABLE I. Suspension data: lab code and/or manufacturer's batch no.; references for the kinetic data; diameter with experimental method indicated. UZ: Ultracentrifuge measurements performed by the manufacturer; TEM: transmission electron microscopy; polydispersity index PI [Standard deviation normalized by mean diameter, values given refer to diameters and standard deviations measured with the methods indicated. Additional measurements employing USAXS form factor measurements, static light scattering and dynamic light scattering gave values agreeing within some 5–7% with the values quoted; see text for further details.]; effective charge number, $Z_{\mathrm{eff},G}$ from elasticity measurements; dimensionless effective surface potential, Ψ_{eff}, assuming the effective charge saturation limit; freezing (F) and melting (M) number densities from static light scattering; nearest neighbor spacing d_{NN} at melting in microns; and in terms of the particle diameter.

Sample batch no.	Ref.	$2a$/nm	PI	$Z_{\mathrm{eff},G}$	Ψ_{eff}	$n_F/\mu\mathrm{m}^{-3}$	$n_M/\mu\mathrm{m}^{-3}$	d_{NN}/μm at melting	$d_{NN}/(2a)$ at melting
PNBAPS68 BASF ZK2168/7387	[30,54,55]	68 (UZ)	0.05	331 ± 3	9.5	6.0 ± 0.3	6.1 ± 0.3	0.55	8.1
PNBAPS70 BASF GK0748	[56]	70 (UZ)	0.043	325 ± 3	8.6	1.8 ± 0.2	2.0 ± 0.2	0.79	11.2
SI77	[11]	77 (TEM)	0.08	260 ± 5	6.4	$> 28 \pm 1$	30 ± 1	0.32	4.1
PS90 Bangs Lab 3012	[31]	90 (TEM)	0.025	315 ± 8	8.1	4.0 ± 0.5	4.6 ± 0.5	0.60	6.7
PS100B Bangs Lab 3067	[31]	100 (TEM)	0.027	327 ± 10	7.6	4.2 ± 0.5	5.5 ± 0.2	0.57	5.7

HS polycrystal-fluid interface [83]. They obtained a value of $\sigma_{0,HS} = (0.58 \pm 0.05) k_B T$ for the reduced equilibrium IFE. This value is in close agreement with theoretical expectations and simulation results which—depending on the approach taken—give orientationally averaged values of the reduced equilibrium IFE, $\sigma_{0,HS} = (0.56\text{–}0.68) k_B T$ [64,66,68–73].

More recent work also addressed body centered cubic (bcc) crystal structures in contact with their melt. Heinonen *et al.* studied crystallizing point Yukawa systems, comparing state-of-the-art molecular dynamics simulations and theoretical approaches [84]. For this particular kind of long ranged repulsive electrostatic interaction, the authors obtained IFEs which were much lower than those of HSs. Also for bcc-crystallizing metals, a few simulation studies have been reported [85]. In these studies, IFE values are on the same order as those of fcc or hexagonal close-packed (hcp) metals [85,86], but their IFE anisotropy and temperature dependence as well as Turnbull's coefficient are predicted to be considerably smaller than for fcc metals.

A second set of data was obtained in studies on nonequilibrium clusters using CNT to extract effective IFE values from their nucleation rate densities. Data are available for both atomic systems [41,45,46,51,52,87] and colloids [24,29,34–36,63,65,88–90]. The nonequilibrium CNT-based effective IFEs for the hard sphere colloids agree with the values obtained under equilibrium conditions with reduced values of about $\sigma \cong 0.55 k_B T$. This is particularly true for those values obtained at the melting volume fraction [24]. Concerning metals, we note that experimental data obtained at the nucleation temperature of metals, T_N, may be converted to estimates of the effective IFEs at the equilibrium melting temperature, T_M. This has been demonstrated, e.g., in the case of Ni in a combined study of calorimetrically obtained nucleation rates and state-of-the-art simulations [91]. There, a near quantitative agreement of the estimated values with the values measured for the same system at equilibrium was observed [86]. To perform these estimates and conversions for systems with dominant hard-core interaction, a constant entropy of freezing appears to be a sufficient assumption [53]. More sophisticated corrections including size dependence of the IFE and the temperature dependence of the enthalpy of freezing have been discussed in [43]. This large data compilation further suggests that Turnbull's coefficient remains unaffected by the mentioned conversion, i.e., it can equally well be read from the reduced nonequilibrium IFE at the nucleation temperature and the equilibrium IFE at the melting temperature. Interestingly, the CNT-based effective nonequilibrium IFEs, the interfacial stiffnesses, and their temperature dependencies are found to be much smaller in the bcc than in the fcc case, when compared for the same interaction type and strength. Also, in a recent extensive simulation of nucleation in hard-core Yukawa systems the nonequilibrium IFE was found to be a factor 2 smaller in the case of bcc crystals as compared to the case of fcc crystals [17]. This observation is also theoretically supported within the negentropic model of Spaepen *et al.* [92,93] and the broken bond model of Gránásy and Tegze [94]. Thus, also Turnbull's coefficient C_T should take different values for different structures. In fact, experimental values for C_T of fcc crystallizing metals converge to $C_{T,fcc} = 0.43$ [46] while simulation results for fcc crystallizing metals are better described by $C_{T,fcc} = 0.55$ [85]. The few simulation results available for bcc-crystallizing metals are best described by $C_{T,bcc} = 0.29$ [85]. Our first systematic estimate of $C_{T,bcc,\mathrm{expt}} = 0.31 \pm 0.03$ appears to be much smaller than the values found for fcc crystallizing systems and is in remarkably close agreement with predictions for bcc systems.

The comparison of theoretical and experimental results faces yet another difficulty in that the bulk of theoretical IFE studies focused on strictly monodisperse systems. By contrast, all experimental studies on colloids have to cope with an inevitable polydispersity, characterized by a polydispersity index, PI $= s_a/\bar{a}$, where $\bar{a}$ is the mean particle radius and s_a is the standard deviation. Data considered in the present paper were taken on samples of different PIs ranging 0.025–0.08.

Interestingly, in their simulations on the crystallization of polydisperse HS, Auer and Frenkel found both the (expected) decrease of the nucleation barrier with increased metastability but moreover observed an increase with increased polydispersity. This increase occurred for PI > 0.05 and was interpreted in terms of an increase of IFE with increasing PI [88]. On the experimental side, Schöpe *et al.* reported a dramatic slowing of the onset of nucleation, but at the same time also an increase in nucleation rate densities for HS systems, when the PI was increased by a mere percent from 0.048 to 0.058 [95]. These authors discussed their findings as indicative of the onset of fractionation processes. The latter are expected to occur for PI $\geqslant 0.05$ [96–99] and are also observed for eutectic binary mixtures of HSs and attractive HSs [32,100–102]. They are also predicted and observed for charged particles but at much larger PI [103,104]. Therefore, the PI seems to have a strong influence on nucleation kinetics. But the important open question that remains is how IFEs react to polydispersity particularly at comparably low values of PI, where fractionation effects are expected to play a subordinate role. Having access to a large number of systems differing with respect to polydispersity, we are able, for the first time, to look at its influence in a more systematic way. We find that the IFE systematically decreases with increasing polydispersity, while the Turnbull coefficient remains unaffected.

The remainder of the paper first will quickly recall the characteristics of the investigated samples, the experimental procedures, and the evaluation schemes leading to the reported nonequilibrium IFEs. We then will determine the $\sigma_{0,bcc}$ for the five pure species and one binary mixture from a simple extrapolation scheme. In an extension of this scheme, we will further estimate other thermodynamic quantities including Turnbull's coefficient. We continue with an extensive discussion of our findings, where we address the observed values and their spread, the observed anticorrelation of σ_0 to the PI, and the observed Turnbull coefficients for bcc-crystallizing systems. After that we will give our conclusions. There are several appendixes that provide more background information on (A) additional correlation checks, (B) the characterization of particle interactions under deionized conditions, (C) the determination of CNT-based effective nonequilibrium IFEs from nucleation and growth measurements, and (D) the use of CNT and related schemes to obtain nonequilibrium IFEs.

II. ANALYZED SYSTEMS AND THEIR CHARACTERISTICS

A. Particle characterization

We start with shortly recalling the characteristics of the investigated systems and the methods employed in obtaining the nonequilibrium IFE. A more detailed discussion of the experiments and raw data interpretation can be found in Appendix C. We analyze data of five species of moderately to highly charged colloidal spheres in aqueous suspension and one binary mixture. Copolymer particles were kindly provided by BASF, Ludwigshafen. Silica particles were homemade employing Stöber synthesis. Systems under consideration are compiled in Table I with the corresponding references for the measurements of the nucleation rate densities [11,30,31,54–56]. Sample laboratory codes refer to the particle material (polystyrene: PS; poly-n-butylacrylamide: PNBA; silica: Si) and particle diameter (in nm).

For the present investigation, size characterization is of prime importance. Si and PS diameters were obtained from Transmission Electron Microscope (TEM) images with the PS data quoted from the manufacturer. Ultrasmall angle x-ray scattering (USAXS) form factor measurements on the Si particles gave coincident values. PS particles were further investigated by static light scattering returning slightly larger values for the geometric radii, indicating a slight shrinkage of particles under TEM conditions. They were also investigated by dynamic light scattering returning hydrodynamic radii which are larger than the geometric radii by some 5%. The copolymer particles are not stable under the TEM. Their diameters were determined by the manufacturer from ultracentrifugation. Here, static light scattering gave slightly smaller diameters (by about 1.5%), dynamic light scattering again gave some 5% larger values. While this spread in diameters reflects the (known) differences between the applied methods [105], this study is primarily interested in the corresponding polydispersities. Using TEM, some 1500 particles were counted for each species. Form factors from USAXS and static light scattering were analyzed using a polydisperse Mie fit [106], dynamic light scattering was analyzed using the cumulant method. In each case the statistical uncertainties of the standard deviation of the diameters are estimated to be below 10%, with the lowest uncertainties for the analytical ultracentrifugation and the largest for the cumulant method. However, for ultracentrifugation an additional systematic uncertainty arises from the use of the bulk PnBAPS-copolymer density, as does for static light scattering from modeling the particles as homogeneous spheres utilizing the bulk index of refraction. The combined statistic and systematic uncertainty in the PI are therefore dependent on the choice of method to determine the average diameter. A conservative estimate gives 15% uncertainty as an upper limit for the PIs shown in Table I. Interestingly, however, for each species, the PI values obtained by different methods agreed within 5% to 7% .

Size polydispersities range from low (PI $= 0.025$) to moderate (PI $= 0.08$). These values are the geometric polydispersities, which hardly alter the interparticle spacing and thus the strength of pair interactions. For charged spheres, however, one expects an additional charge polydispersity, altering the pair interaction at d_{NN}. For highly charged low salt systems, like the ones investigated, a suitable analytic expression for the effective pair interaction is given by a Debye-Huckel pair potential with a renormalized effective charge [107–110] which scales linearly with the particle radius [111] (see also Appendix B). Thus any size polydispersity directly translates into a charge polydispersity. However, little is known about the effects of charge polydispersity on the properties of charged sphere suspensions, with the exception that effects on the phase behavior are smaller in CS than in HS systems with the same PI [112]. In fact, a procedure proposed by Löwen *et al.* [113] to map charge PIs to HS size PIs gave some 50% smaller values in the latter case. Unfortunately, this procedure is not reliably applicable for the present highly charged low salt systems [114]. In a recent study, van der Linden *et al.* showed that the maximum PI compatible with crystal formation without fractionation is about 0.13 [103] which is to be compared to

the maximum PI of about 0.062 in the HS case [97]. Similarly, no fractionation effects are observed for any of our single component systems and furthermore the mixture crystallizes as bcc substitutional alloy with a spindle type phase diagram [115], whereas binary mixtures with HS-like interactions would form a eutectic at this geometric size ratio [116]. We therefore note that the given PIs should be taken as upper limit and that the effective PIs are probably much smaller.

All particles are negatively charged and were investigated under thoroughly deionized conditions using advanced, continuous ion exchange techniques [117]. For further details of the preparation procedure and the characterization of the interaction strength and range under deionized and strongly interacting conditions, the interested reader is referred to Appendix B. We assume to have the highly charged particles in or close to the effective charge saturation limit [109,110] and calculate the dimensionless effective surface potential $\Psi_{\text{eff}} = Z_{\text{eff},G}\lambda_B/a$ as a measure of interaction strength [107,108]. Here a is the particle radius, $\lambda_B = 0.72$ nm is the Bjerrum length in water and $Z_{\text{eff},G}$ is the effective charge from elasticity measurements [118]. In the deionized state, all samples including the mixture form polycrystalline bcc solids for $n \geqslant n_F = 2$–$8\ \mu\text{m}^{-3}$ with the location of the melting line coinciding with theoretical expectations [115,119,120].

B. Crystallization experiments and determination of nonequilibrium IFEs

Use of the continuous deionization technique cycling the suspension in a closed tubing circuit keeps the systems in a homogenized shear-molten state prior to resolidification [117]. Growth measurements were performed in rectangular cells with the growing wall crystals observed by Bragg microscopy [34]. For all samples and $n > n_M$, growth was observed to be strictly linear in time, characteristic of reaction limited growth. The number density dependent growth velocity v was interpreted in terms of a Wilson Frenkel growth law to obtain an estimate of the difference in chemical potential between melt and crystal, $\Delta\mu$. This was done for PnBAPS68, PnBS70, PS100B, and Si77 by fitting a modified Wilson-Frenkel expression which, following Würth, was based on a reduced energy density difference calculated with a density dependent interaction potential [62]. For PS90, no growth data were available at the time of publication of the nucleation rate densities [31]. Therefore a simple estimate for $\Delta\mu$ was used based on the reduced density difference: $\Delta\mu = B(n - n_F)/n_F$ with the proportionality constant reported by Aastuen *et al.* for particles of 91 nm size: $B = 10$ [61]. Later, measurements of the growth velocity in dependence on particle concentration were made for PS90. The modified Wilson-Frenkel fit of these data using Aastuen's expression returned a proportionality constant of $B_{PS90} = 4 \pm 0.6$ ([121], see also Appendix C). Since also the evaluation of PS100B growth data using Aastuen's approximation yielded a value of $B = 4.0 \pm 0.2$, we choose to adapt a value of $B = 4$ for the mixture, too.

The nucleation rate density J varies drastically with increasing n. Therefore, different techniques were employed in its study. At low densities, J was determined directly from videomicroscopy in Bragg-microscopic mode [34,54], at medium densities via past-solidification size counts from polarization microscopy [56], and at high densities from Bragg scattering or time resolved USAXS measurements [11,30,31,55]. All three approaches yield consistent $J(n)$ for a given sample. For CS, $J(n)$ first increases near exponentially with increasing n, then the increase gradually slows, but no decrease like the one known from HSs is observed (for a comparison see, e.g., [31] and Appendix C). From the combined data sets of $J(n)$ and $\Delta\mu(n)$ the nucleus-melt interfacial free energies $\gamma(n)$ were derived in the framework of CNT. Either we performed a least-square fit of Eq. (C8) to the data using a proportionality constant A, an effective long time self-diffusion coefficient $D_L^S(n)$ and $\gamma(n)$ as free parameters, or a graphical evaluation method was utilized in which $\gamma(n)$ was determined from the local slope more directly without any assumption about the kinetic prefactor (for details see [30,55] and Appendix C). For PS90 and the mixture the original nucleation data were re-evaluated using $B = 4k_BT$ to return slightly altered IFEs and a significantly increased dependence on $\Delta\mu$.

In Fig. 1 we replot the data reported for PnBAPS68, PnBAPS70, Si77, and PS100B together with the corrected data for PS90 and the 1:1 mixture of PS90 and PS100B in terms of their reduced values $\sigma = \gamma(\Delta\mu)d_{NN}{}^2$. The data sets show different uncertainties. In particular for Si77, graphical evaluation led to an enlarged statistical uncertainty in σ. Furthermore, estimating $\Delta\mu$ following Aastuen and neglecting the density dependence of the interaction potential results in an enhanced systematic uncertainty in $\Delta\mu$ for PS90 and the mixture. Note that this will influence only the slope but not the intercept of any linear fit since the freezing point with $\Delta\mu = 0$ is accurately known. For the other samples, γ was determined from fits of classical nucleation theory expressions [55] and $\Delta\mu$ was determined from growth experiments following [62]. There, the uncertainties are mainly statistical and remain on the order of a few percent.

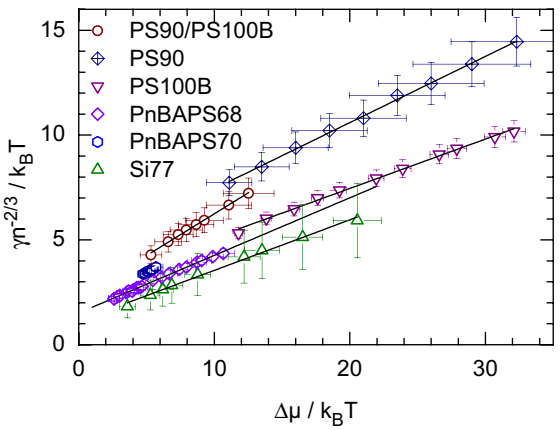

FIG. 1. Dependence of the reduced interfacial free energies on metastability $\Delta\mu$ for the indicated species. Interfacial free energies γ (in J/m^2) were normalized by $n^{-2/3}$ and plotted in units of k_BT as quoted from the original literature or re-evaluated from the original data using a corrected value for $\Delta\mu$. Solid lines are least-square fits of $\sigma = \sigma_0 + m\Delta\mu$. Note that here and throughout, we adopt the convention to consider the crystal as educt and the melt as product, as to obtain positive values for $\Delta\mu$, ΔH_f, and ΔS_f.

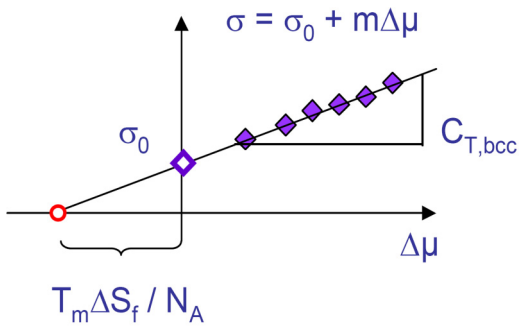

FIG. 2. Extrapolation scheme based on Turnbull's rule: $\sigma_0 = C_T \Delta H_f / N_A = C_T T_M \Delta S_f / N_A$.

III. DATA ANALYSIS AND RESULTS

A. Equilibrium IFEs and their dependencies on system parameters

Figure 1 reveals that, within experimental error, the reduced nonequilibrium IFEs of all charged sphere samples show a strictly linear increase for increasing metastability. This suggests the use of the scheme sketched in Fig. 2 and we simply extrapolate the data to zero $\Delta\mu$ without making any further assumptions. We obtain the extrapolated equilibrium IFE and the slope by performing least-square fits of $\sigma = \sigma_0 + m\Delta\mu$. The results for σ_0 and m are displayed in Table II.

Note that the obtained σ_0 range between $1.13 k_B T$ and $4.23 k_B T$, i.e., a large spread of values, is obtained for the different samples. With a thorough system characterization at hand, we check correlations of the obtained σ_0 to other quantities. In Figs. 3(a)–3(e) we plot the data versus (a) the effective charges $Z_{\mathrm{eff},G}$, obtained from elasticity measurements for the crystal phase over the range of interest; (b) the number-averaged mean particle diameter $2a$; (c) the dimensionless effective surface potential Ψ_{eff}; (d) the effective temperature, $T_{\mathrm{eff}} = k_B T / V(d_{NN})$, as calculated using $T = 298$ K and the effective interaction strength at the nearest neighbor site [cf. Eqs. (B1) and (B2)] for the conditions encountered at melting; and (e) the value of the coupling parameter $\lambda = \kappa d_{NN}$ at melting. No clear correlation is observable in any of these cases.

Next we plot σ_0 versus the polydispersity index, PI, in Fig. 4. Here, a clear decrease of σ_0 with increasing polydispersity is observed. Further, PS90 and PS100 show σ_0 of $(4.28 \pm 0.43) k_B T$ and $(2.75 \pm 0.11) k_B T$, respectively. If mixed 1:1 by number, σ_0 of the PS90-PS100B mixture drops to $(2.26 \pm 0.16) k_B T$ which is significantly lower than the value observed for either pure system. Figure 4 thus shows that the equilibrium values of the reduced IFE as extrapolated from the CNT-based effective nonequilibrium IFEs are anticorrelated to the polydispersity of the investigated systems. This is a central result of the present paper.

As shown in Appendix A, the slope m behaves differently and shows neither a correlation to any of the interaction parameters nor to the polydispersity index.

B. Estimates for $C_{T,bcc}$, ΔH_f, and ΔS_f

Our scheme can also be used to extract estimates of further important quantities by making additional assumptions. First, we assume that the molar entropy of freezing does not change with increasing metastability, i.e., with increasing particle number density. This has been shown to apply for HSs [53] and further has been observed for many metal systems [43]. Both are systems where the hard-core repulsion creates an excluded volume which is dominating the behavior of the condensed phase. In the present systems with their electrostatic interaction, the interaction is much softer, but still the repulsive part dominates the observed ordering processes. Second, we assume that Turnbull's rule which was found for metals also applies in the colloidal case: $\sigma = C_T \Delta H_f / N_A$, where N_A is Avogadro's number. With these assumptions made, we further note that at $\Delta\mu = 0$, $\Delta H_f / N_A = T_M \Delta S_f / N_A$. With $\Delta S_f / N_A = \text{const}$ and $\sigma = C_T \Delta H_f / N_A$ this implies that at $\sigma = 0$, $\Delta H_f / N_A = 0$ and $\Delta\mu = -T_M \Delta S_f / N_A$, where the melting temperature in our systems is identified with the ambient temperature $T_M = 298$ K. Therefore, extrapolating the data to the intercept with the $\Delta\mu$ axis yields an estimate of the entropy of fusion and the enthalpy of fusion at equilibrium. Finally, the slope of the curve $m = \sigma_0 / (T_M \Delta S_f / N_A)$ can be identified to Turnbull's coefficient $m = C_T$. This latter identification was suggested by P. Wette, in his Ph.D. thesis [122] and was later used in [11,33]. Values for $m = C_{T,bcc}$ are shown in Table II. They range between 0.235 and 0.405, each with small statistical uncertainties reflecting the good linear correlation of σ and $\Delta\mu$. The spread of values is smaller that that observed for σ_0 and no clear correlation between σ_0 and $C_{T,bcc}$ is found [see Fig. 7(a) in Appendix A]. Moreover, none of the tests for correlations of $C_{T,bcc}$ to particle or system quantities gave any significant results [see Figs. 8(a)–8(f) in Appendix A]. In particular $C_{T,bcc}$ is observed to be uncorrelated to the PI.

The values of molar ΔS_f and ΔH_f are also compiled in Table II. Those for ΔS_f range between 1.5 and 4.6 J mol^{-1} K^{-1} and those for ΔH_f range between 0.45 and 1.36 kJ mol^{-1}. Correlation checks show that, like σ, $T\Delta S_f$ (respectively ΔH_f) is not correlated to Z_{eff}, $2a$, Ψ_{eff}, T_{eff}, or κd_{NN}. By contrast, an anticorrelation is observed to the PI. Like σ_0, $T_M \Delta S_f$ shows a clear trend to decreases with increasing

TABLE II. Results for a fit of $\sigma = \sigma_0 + m\Delta\mu$ to the data shown in Fig. 1. We obtain the intercept, i.e., equilibrium reduced IFE, σ_0, and the slope m, i.e., the Turnbull coefficient $C_{T,bcc}$. Further, we show estimates of the the molar entropy of fusion ΔS_f and the molar enthalpy of fusion ΔH_f.

	PnBAPS68	PNBAPS70	Si77	PS90	PS100B	PS90/PS100
$\sigma_0 / k_B T$	1.51 ± 0.04	1.62 ± 0.07	1.13 ± 0.16	4.28 ± 0.43	2.75 ± 0.11	2.26 ± 0.16
$m = C_{T,bcc}$	0.274 ± 0.003	0.364 ± 0.018	0.254 ± 0.008	0.316 ± 0.005	0.235 ± 0.005	0.405 ± 0.011
ΔS_f/J mol^{-1} K^{-1}	1.85 ± 0.1	1.51 ± 0.13	1.58 ± 0.17	4.56 ± 0.47	3.93 ± 0.27	0.57 ± 0.05
ΔH_f/kJ mol^{-1}	0.55 ± 0.3	0.45 ± 0.4	1.36 ± 0.14	1.17 ± 0.8	1.17 ± 0.8	0.57 ± 0.05

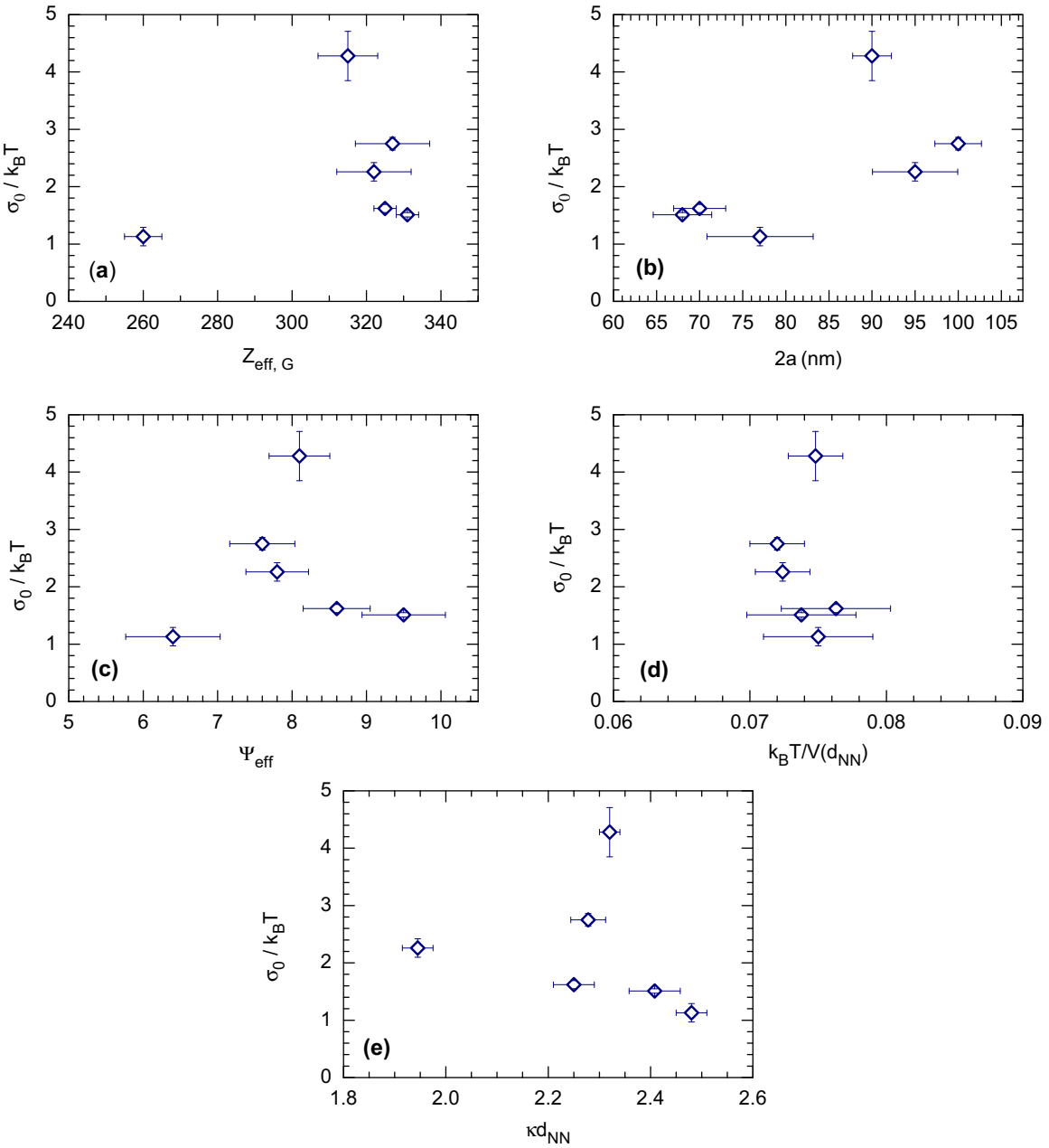

FIG. 3. Correlations between the extrapolated reduced equilibrium IFEs and various particle characteristics. (a) Effective charges $Z_{\mathrm{eff},G}$; (b) the number averaged mean particle diameter $2a$; (c) effective surface potential Ψ_{eff}; (d) effective temperature, $T_{\mathrm{eff}} = k_B T / V(d_{NN})$, at melting; (e) coupling strength at melting. No clear correlation of σ_0 to any of these interaction parameters is obtained.

PI and again the value for the mixture is well below that of the pure components [see Fig. 7(b) in Appendix A]. To highlight this finding, we plot in Fig. 5 the correlation of σ_0 to $T_M \Delta S_f = \Delta H_f$ and observe a clear linear correlation with slope $b = 2.76 \pm 0.19$ and a correlation coefficient of $r = 0.988$.

To summarize the results of our extended analysis of CNT-based reduced nonequilibrium effective IFEs, we find that deionized charged sphere suspensions of different charge, size, and polydispersity show extrapolated equilibrium reduced IFEs which are (i) in the range of a few $k_B T$, (ii) systematically increasing with increased metastability expressed as $\Delta\mu$, (iii) not correlated to any of the interaction parameters, but (iv) linearly correlated with the entropy of fusion, and (v) as the latter, decreasing with increasing polydispersity.

IV. DISCUSSION

The above results call for further discussion of a number of points. We first discuss the observed values and their spread, then turn to the observed anticorrelation of σ_0 to the PI, and finally comment on the observed Turnbull coefficients for bcc-crystallizing systems.

The magnitude of the observed equilibrium reduced IFEs may appear unexpectedly large. Values range between $1.25 k_B T$ and $4.4 k_B T$. In Fig. 4, we compare it to values

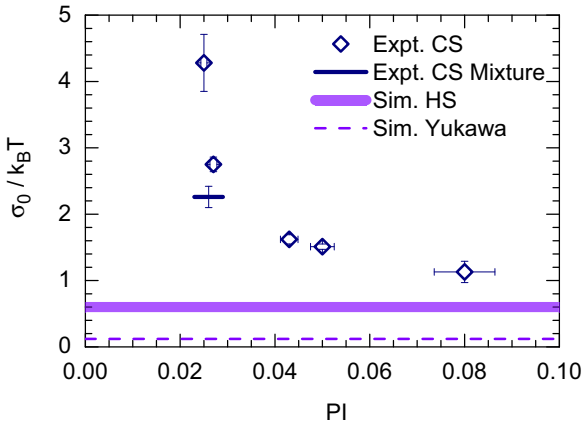

FIG. 4. Correlation between the extrapolated reduced equilibrium IFEs and the polydispersity index PI. A clear anticorrelation is observed: σ_0 decreases with increasing PI for all single component samples. The case of the mixture is denoted by the horizontal bar. Its length and position denote the range of PIs covered by the involved single component samples. Note that its position does not correspond to the effective PI of the bimodal size distribution of the mixture. This quantity would be much larger, but cannot be obtained from the equation for monomodal PIs: PI $= s_a/\bar{a}$. Note further that its value lies significantly below those of the corresponding single component species. For comparison, we also show values for the equilibrium IFE as obtained from simulations of macroscopic flat fluid-crystal interfaces of monodisperse HSs (solid horizontal line with thickness corresponding to the spread of published data) and a point Yukawa system (dashed line). (For further details, see text.)

observed for other systems. The lowest values reported so far were obtained for the point-Yukawa system by Heinonen *et al.* [84] as $\sigma_{0,bcc,\text{Yukawa}} = (0.12 \pm 0.02)k_BT$ (dashed line in Fig. 4). These authors further mention unpublished work, where they obtained $\sigma_{0,fcc,\text{Yukawa}} = 0.4k_BT$ (Ref. [46] in [84]), whereas their value obtained using the same methods for HSs was $\sigma_{0,fcc,HS} = 0.65k_BT$. Auer and Frenkel have given

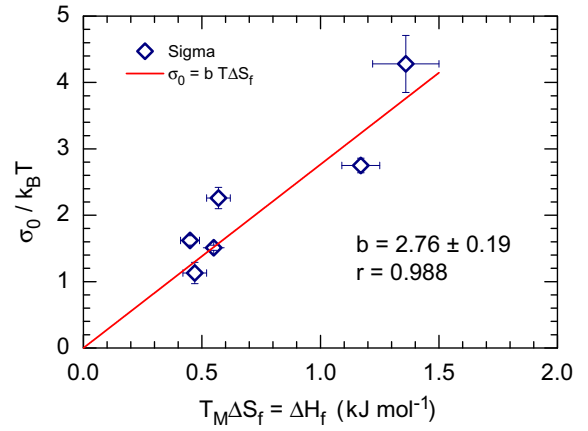

FIG. 5. Correlation between the extrapolated equilibrium reduced IFE and the enthalpy of fusion equaling the entropy of fusion times the melting temperature. A good linear correlation (correlation coefficient $r = 0.988$) is observed as expected from Turnbull's rule and its interpretation by Laird [41,53].

CNT-based estimates of nonequilibrium IFEs from their Monte Carlo simulations of slightly charged hard spheres modelled by a repulsive hard-core potential [65,90] which are $\gamma(2a)^2 = 0.45k_BT$ in the case of fcc and $\gamma(2a)^2 = 0.38k_BT$ in the case of bcc crystals. Normalization with d_{NN}^2 would have resulted in somewhat larger values for the reduced nonequilibrium IFEs. However, given the experimentally observed dependence of σ on metastability, one would expect the equilibrium values to be much smaller than the reported nonequilibrium values, possibly close to those found by [84]. In any case, these values are considerably smaller than values reported for HS and the extrapolated IFEs reported here.

In Fig. 4, we also display the range of values reported for the HS reference system, $\sigma_{0,fcc,HS} = 0.56$–$0.68k_BT$ (thick horizontal line). We note that CNT-based effective IFEs [24,29,34–36,63,90] and equilibrium IFEs [64,66,68–73,82,83] do not show significant differences and are all significantly below the values observed here for the case of CS.

Metals on the other hand show values of 20–400 mJ/m^2 at their nucleation temperature. When scaled to T_M and the area taken by a single atom in the interface, this results in values of several to some tens of k_BT for $\sigma_{0,fcc,\text{metal}}$ [41,43–46,52,85]. Of particular interest is the recent comparison of nucleation barriers of Ni derived *via* CNT from nucleation experiments to those derived from state of the art Monte Carlo simulations on the nucleating system [91] which quantitatively coincide in the case of sufficiently large simulated systems. Further, a mere 10% discrepancy is observed between the derived nonequilibrium IFEs scaled to the melting temperature and the equilibrium values derived from simulations of the equilibrated interface [86].

A good agreement is thus observed between CNT-based effective IFEs and the more directly measured equilibrium IFEs for HS and metals, while the present CNT-based effective IFEs of polydisperse CS differ from the equilibrium IFEs obtained for Yukawa and hard-core Yukawa systems. Thus either CNT is not very reliable in our case or mean field descriptions are not suitable to predict IFEs for the systems used in our experiments, even though Yukawa and hard-core Yukawa potentials quantitatively capture the interaction strength and range.

Our comparison reveals a pronounced sorting in groups of different interaction type. In principle, also the significant spread within the group of charged colloids (and that of metals) can be due to differences in interaction type, strength, and/or range. However, as seen in Figs. 3(a)–3(e), there is no significant correlation between σ_0 and any of the interaction parameters. On the other hand, we observed a clear anticorrelation between σ_0 and the PI in Fig. 4 and a linear correlation of σ_0 to $T_M\Delta S_f$ in Fig. 5. It should be noted that already in his seminal paper [52], Turnbull observed σ_0 to be correlated to the melting temperature T_M of the investigated elements. However, due to the rather large overall scatter of these data, this observation was discarded as a basis to formulate an empirical relation. Rather, the clearer correlation to $\Delta H_f/N_A$ was used. Later, Laird theoretically investigated the IFE of hard-core systems to observe a clear scaling of the metal σ_0 with T_M [53]. This correlation is also present in the much larger data compilation published by [43]. Laird pointed out that this scaling is a direct consequence of

the purely entropic determination of the phase behavior of HSs and the presence of a hard-core-like repulsion in metals. Earlier, Saepen and co-worker [92,93] similarly argued that given a structure specific but otherwise constant entropy of fusion, the IFE should vary linearly with temperature upon undercooling a melt. This is also seen for the present systems, where σ_0 varies linearly with $\Delta\mu$ which may be regarded as the colloid analog of undercooling. Therefore, we believe that the presently observed large values for σ_0 are caused by a large entropy difference between melt and crystal and furthermore, that the spread is caused by a polydispersity-induced variation of this difference.

We may rationalize this, considering a monodisperse system transforming from a melt of short range order to a crystalline state of long range order. Introducing some polydispersity will disturb both phases differently. There will be a structural change (a deviation from the best ordered low energy or low entropy configuration) which is different for the polydisperse crystal and for the polydisperse melt. Loosely speaking, the order of the melt will be disturbed only over short distances, while the disturbance in the arrangement of particles in the crystalline state will be long ranged. In both cases, the entropy of the less well ordered region will increase, but, due to the rules of combinatorics, the effect of the larger number of particles involved in the distorted crystal is far larger. Therefore, in the polydisperse case, the entropy difference between the two phases will be smaller than in the monodisperse case. Consequently, also σ_0 has to decrease, and we observe the samples with the largest PI to display the lowest IFE. We note that the results shown in Figs. 4 and 5 may be considered as an independent test of Turnbull's rule using model systems of different polydispersity yielding an *a priori* unknown, but systematic decrease of entropy differences.

We come back to the discrepancies observed in comparing our IFEs to those of simulated point and hard-core Yukawa systems. For the presently examined case of experimental charged spheres with their additional Z_{eff} counterions per particle, the entropy difference between melt and solid should be much larger than for any HS, point Yukawa, or hard-core Yukawa system. In this latter cases, either counterions are not present or are absorbed in a neutralizing mean field background. Therefore, any counterion contribution to the entropy is neglected in these systems. In principle, this hypothesis can be tested by theoretical investigations within the primitive model that may become feasible with state-of-the-art algorithms [17]. Moreover, with this data available also a comparison of the presently derived CNT-based effective IFEs and more directly measured equilibrium IFEs will become possible.

Crystallization of colloidal suspensions may involve fractionation processes. The PIs of the present systems ($0.025 \leqslant \text{PI} \leqslant 0.08$) are considerably lower than those for which fractionation is expected and/or found in CSs [103,104]. Further, in none of the experiments were the characteristic broad, pyramid-shaped Bragg peaks observed [101]. Moreover, in deionized CS binary mixtures, the size ratios for stabilizing azeotropic or eutectic phase behavior are shifted to much smaller values as compared to HSs [123]. Therefore, we believe that the effective CS polydispersities are considerably lower than the geometrical ones, and we exclude fractionation effects for the present systems. However, in accordance with theoretical expectations [96–99], fractionation has been observed in strongly polydisperse experimental HS systems [101,124].

Fractionation has also been observed in the simulations of Auer and Frenkel [88,90]. They reported an increase of the nucleation barrier with increasing PI for $\text{PI} > 0.05$ which was attributed to an increase in IFEs. This seems to be at odds with the present observation of a clear nonlinear decrease of σ_0 with increasing PI (cf. Fig. 4). However, fractionation affords the formation of purified phases of much lower entropy than the melt or the substitutional crystal [100]. For the purely entropic HS system, this will increase both γ and $\Delta\mu$ between the fractionated crystal nucleus and the remaining melt. Consequently, the nucleation barrier $\Delta G^*_{CNT} = (16\pi\gamma^3)/3(n\Delta\mu)^2$ will increase with increasing PI. This effect limits the range of applicability of our conclusions to nonfractionating systems. The presently observed decrease of σ_0 with PI should be reversed at the onset of fractionation, and the IFE should display a minimum as a function of PI. The situation is further complicated by the fact that fractionation will also influence the kinetic prefactor. The required sorting processes decrease the kinetic prefactor, and contribute to the observed drastic slowing of nucleation [32,100]. The findings by Schöpe [95] may have been made in a crossover region, where the decreased kinetic prefactor already caused considerably stretched induction stages, while the effects on the barrier were not yet pronounced enough to quench nucleation effectively. However, the issue of the influence of fractionation is far from being generally settled. It should be addressed again in both simulation and experiments on nonfractionating HS systems as well as fractionating CS systems.

We further compare the values of the other estimated thermodynamic quantities to those for other systems. Our absolute values for molar ΔH_f range between 0.45 and 1.36 kJ mol^{-1}. This is just below those of alkaline metals, which range about 2–3 kJ mol^{-1}, but smaller than the values of about 8 kJ mol^{-1} for alkaline earth metals and 35.2 kJ mol^{-1} for tungsten [125]. Values for ΔS_f range between 1.5 and 4.6 J mol^{-1} K^{-1} as compared to a value of about 10 J mol^{-1} K^{-1} for metals. For monodisperse HSs, density functional theory calculations yield 9.7 J mol^{-1} K^{-1} [53]. The values for polydisperse CSs are thus much smaller than those of monodisperse systems with shorter-ranged interactions. Therefore, it would be interesting to pursue this case further in two ways. One way is to investigate nucleation in charged sphere suspensions at larger particle and salt concentrations, where the interaction potential becomes less soft. The second way would be investigations using CSs with vanishing PI.

Finally, we have used the identification of the fitted slope m to Turnbull's coefficient $C_{T,bcc}$. From this, we obtained systematic estimates for this quantity for a set of experimental systems crystallizing into bcc structure. We note that as expected, the presently observed values are independent of σ_0, of the PI and of the interaction parameters (cf. Appendix A). In fact, the strictly linear dependence of σ on $\Delta\mu$ shows that the very same Turnbull coefficients also apply in the metastable state. Up to now, experimental determinations have only been performed for fcc crystallizing metals, yielding $C_{T,fcc} = 0.43$ [46], while simulation results for fcc

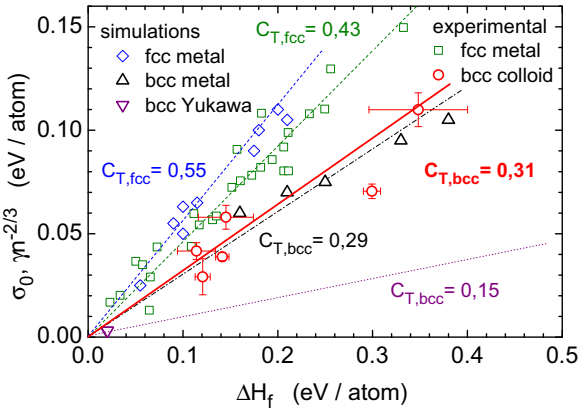

FIG. 6. Turnbull plot of the reduced equilibrium interfacial free energy vs the equilibrium enthalpy of fusion. Shown are our data for bcc-crystallizing colloids (circles), simulation data for bcc-crystallizing metals (up triangles) [85], bcc-crystallizing point Yukawa systems (down triangles) [84], and fcc crystallizing metals (diamonds) [85] as well as experimental data for fcc crystallizing metals (squares) [46]. Lines correspond to the indicated average values of Turnbull coefficients as quoted from [84,85], and [46] for simulation and experimental data, respectively. For our data we find an average value of $C_{T,bcc} = 0.31 \pm 0.03$ (thick solid line) which appears to be remarkably close to that expected for bcc metals.

crystallizing metals are better described by $C_{T,fcc} = 0.55$ [85]. The few simulations available for bcc-crystallizing metals are best described by $C_{T,bcc} = 0.29$ [85]. In Fig. 6 we plot the obtained $C_{T,bcc}$ versus the corresponding reduced equilibrium IFEs (in eV per atom) against the equilibrium enthalpy of fusion (in eV per atom). From an error-weighted linear fit to the data of Fig. 6, we find an averaged Turnbull coefficient of $C_{T,bcc,\mathrm{expt}} = 0.31 \pm 0.03$. Using only the low-uncertainty data with $\Delta\mu$ derived using Würth's approximation for $\Delta\mu$, we obtain a slightly lower value of $C_{T,bcc,\mathrm{expt}} = 0.25 \pm 0.02$. For comparison, we also show the currently available data from the literature. Our values appear to be remarkably close to those from simulations of bcc metals (open triangles [85]) which yielded an average $C_{T,bcc,\mathrm{sim}} = 0.29$ (dash-dotted line) but are much smaller than the values for fcc crystallizing systems. This further supports the theoretical expectations based on entropic considerations that predict that $C_{T,bcc}$ should be considerably smaller than $C_{T,fcc}$ [92–94].

V. CONCLUSIONS

We have analyzed data available from the literature on five pure species and one mixture of charged colloidal spheres obtained from crystallization experiments under deionized conditions. We have devised a simple extrapolation scheme to obtain estimates for the reduced equilibrium IFE from the reduced nonequilibrium CNT-based effective IFEs. Under the additional assumptions of a system specific entropy of fusion which, however, is independent of system density and the validity of Turnbull's rule, we further used this scheme to extract the enthalpy and entropy of fusion, ΔH_f and ΔS_f, as well as the Turnbull coefficient $C_{T,bcc}$. The latter data complement existing experimental and theoretical data on fcc crystallizing systems. The experimental $C_{T,bcc}$ was found to be remarkably close to expectations from simulations on bcc-crystallizing metals. This strongly supports the results of computer simulation and theoretical models predicting a substantial difference in C_T for differing crystal structures.

Incidentally, all analyzed experimental samples showed different degrees of polydispersity. This allowed a discussion of the influence of the PI on both the interfacial free energy and the entropy of freezing. We observed that both quantities show a similar clear trend to decrease with increasing PI and that both quantities are linearly correlated to each other. From this, we conclude that an increase in polydispersity lowers the crystal-melt entropy difference and—consequently—the IFE. Thus, we believe that the thermodynamics of freezing in charged sphere suspensions are dominated by entropic rather than enthalpic effects. At least for the present system, we suggest to reformulate Turnbull's rule in terms of the melting temperature times the gram-atomic entropy of fusion.

The values of the extrapolated IFEs range between those of metal systems and of hard spheres. They show a clear tend to increase with decreasing PI. A PI-dependent IFE has interesting possible consequences for the kinetics of nucleation. If the increase in σ_0 continued for still lower PI, one would expect the nucleation barriers to become very large in the limit of monodisperse charged sphere systems. Then crystallization might become suppressed in favor of a Wigner glass [126]. On the other hand, it may be beneficial to carefully re-investigate the influence of a small geometric polydispersity (for example PI $\leqslant 0.03$) on the nucleation barrier of HS systems. There, state-of-the-art simulations on monodisperse systems in the coexistence region yield nucleation rate densities which consistently are several orders of magnitude lower than those observed in polydisperse experimental systems [36]. If HSs showed a similar dependence of σ_0 on PI as charged spheres, one would expect a small polydispersity to considerably accelerate nucleation.

In most previous work on experimental and computer hard spheres as well as on metals, a near quantitative agreement between CNT-based effective IFEs and those measured more directly on equilibrated interfaces was obtained. Therefore, the observed disagreement between the presently derived results for the CNT-based effective equilibrium IFE and the equilibrium IFE obtained for point Yukawa systems in simulations calls for further attention. Typically, both point Yukawa and hard-core Yukawa based simulations yield good results in predicting charged sphere suspension properties including phase behavior, elasticity, and electrokinetic behavior. A hard-core Yukawa potential has also been employed in the evaluation of the crystallization kinetic data used for the present analysis. Therefore, the reason for the observed discrepancy remains unclear. It may be that the parametrization of measured nucleation rate densities using CNT is not appropriate for the case of CS. However, in view of our main finding that the IFE is mainly an entropic effect, we are tempted to ascribe the discrepancy to the use of Yukawa-type mean field pair potentials in the simulations made. Hence, it will be very interesting to compare our data to future simulations within the primitive model with explicit counterions which may better capture the entropic contributions of the microions.

ACKNOWLEDGMENTS

We are pleased to thank J. Horbach, K. Binder, Th. Speck, Th. Voigtmann, H. Löwen, and H. J. Schöpe for many fruitful, and sometimes critical, discussions. We further thank A. Engelbrecht, R. Meneses, N. Lorenz, I. Klassen, and H. J. Schöpe for providing access to the original data beyond published results, the referees for valuable suggestions, and B. Robertson for reading the manuscript. Financial support by the DFG (Grants No. Pa459/16, No. Pa459/17, and No. He1601/24) is gratefully acknowledged.

APPENDIX A: ADDITIONAL CORRELATION CHECKS

Because the data were available, we performed a number of additional checks for correlations between the obtained key parameters of crystallization and the experimental and system specific boundary conditions.

Figure 7(a) shows that the equilibrium reduced IFE is not correlated to the slope m. This is expected, since also in Fig. 6 and the Turnbull plots found in the literature, C_T is constant irrespective of the measured or calculated σ_0 [41,43,46,52,53,85]. Figure 7(b) shows the correlation between the entropy of freezing and the polydispersity index.

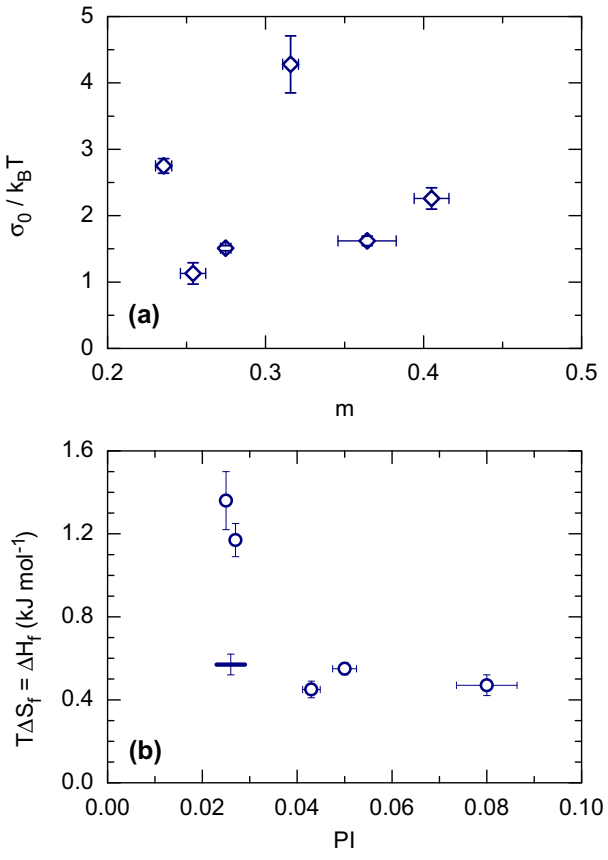

FIG. 7. (a) Equilibrium reduced IFEs σ_0 vs m. No correlation between these two quantities is observed. (b) Plot of $T_M \Delta S_f = \Delta H_f$ vs the polydispersity index PI. A clear decrease is observed. In addition, note the strong decrease also for the value of the mixture (horizontal bar), as compared to those of the two pure components (leftmost circles).

Also here we observe a clear decrease with increasing PI. Note, however, the larger error bars for the cases where $\Delta\mu$ was obtained using the approximation of Aastuen. Its uncertainty translates to an uncertainty in slope and thus in $T\Delta S_f$.

We also checked for any correlations of m to the strength and range of interaction in Figs. 8(a)–8(f). Again the result is negative, possibly with the exception of the weak trend of a decreasing m with increasing coupling parameter κd_{NN} (correlation coefficient $r = 0.53$).

APPENDIX B: CHARACTERIZATION OF PARTICLE INTERACTIONS UNDER DEIONIZED CONDITIONS

Supplied suspensions were first diluted and stored over mixed bed ion exchange resin (Amberlite, Rohm & Haas, France), for a few weeks under occasional gentle stirring. They were then filtered to remove dust, resin debris, and coagulate, regularly occurring upon first contact with the exchange resin. The procedure was repeated using fresh resins. All further conditioning was performed in a closed Teflon(R) tubing system containing a column filled with mixed bed ion exchange resin, a reservoir under inert gas atmosphere, to add particles, water, or electrolyte, a cell for static light scattering to control the particle number density n, a cell for *in situ* conductivity measurements to control the electrolyte concentration, and the actual measuring cell for the crystallization experiments. This procedure allows for a fast and effective deionization and homogenization of the samples. Furthermore it leaves crystallizing suspensions in shear-molten state, from which they readily nucleate and grow crystals, after the shear is stopped. Also the silica species Si77 was first thoroughly deionized, then filled into the circuit and diluted to the desired concentration. NaOH was added up to the equivalence point to obtain maximum charge [11,33].

Under such low salt conditions, van der Waals attraction can be neglected and the pair interaction relevant during solidification experiments is assumed to be a purely repulsive hard-core Yukawa (HCY) potential [127]. Effective electrokinetic charge numbers $Z_{\mathrm{eff},\sigma}$ were determined from the linear particle number density dependence of the conductivity interpreted in terms of a Drude type model [128,129]. These agree well with the charge numbers derived from electrophoresis experiments and charge numbers obtained from the fit of a screened Coulomb potential to the numerical solution of the nonlinearized Poisson-Boltzmann equation within a cell model [110]. The reduction of the effective conductivity charge compared to the bare charge is a consequence of the so-called counterion condensation and in fact gives a measure of the number of freely moving counterions [109]. Furthermore, effective elasticity charges $Z_{\mathrm{eff},G}$ were derived from shear modulus measurements on polycrystalline samples using torsional resonance spectroscopy and interpreting the obtained data in terms of an effective HCY pair potential [118]. In addition to the effects of counterion condensation, this effective charge also accounts for many-body terms in the potential of mean force, the so-called macro-ion shielding [130]. The latter effect is not present for isolated pairs but starts as soon as a third particle is present [131,132]. We note that both effects are due to the overlap of particle electric double layers and that they tend to be fully developed in the case of

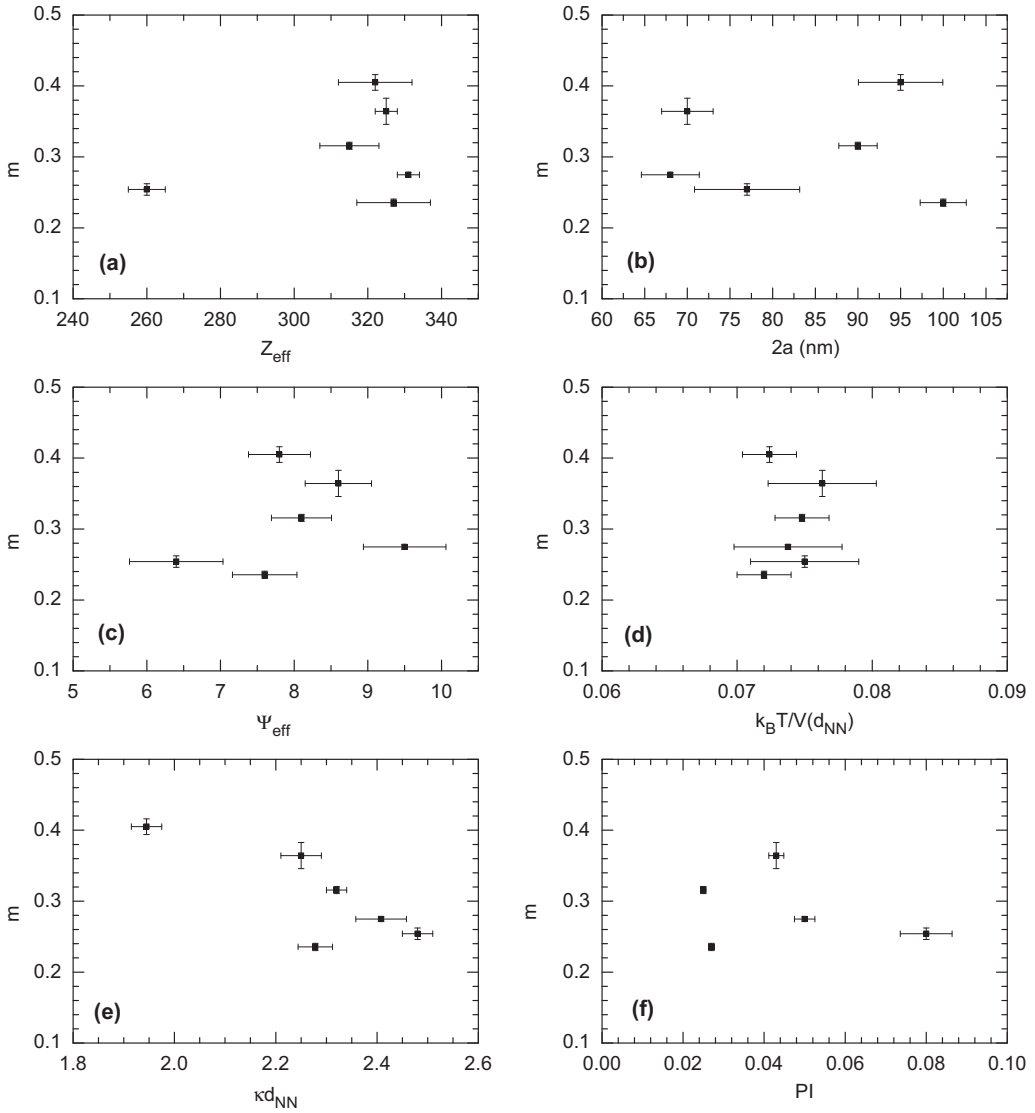

FIG. 8. Correlations between the fitted slope m and various particle characteristics. (a) Effective charges $_{\text{eff},G}$; (b) the number averaged mean particle diameter $2a$; (c) effective surface potential Ψ_{eff}; (d) effective temperature, $T_{\text{eff}} = k_BT/V(d_{NN})$, at melting; (e) coupling strength at melting, κd_{NN}; and (f) polydispersity index PI. Only in (e), a weak correlation is observed with a slightly negative slope and a correlation coefficient of $r = 0.53$. Note that in (f), m does not vary with PI.

counterion dominated screening. For highly charged particles, as used here, counterion dominated screening already develops for densities well below the freezing density and therefore is the case in all crystallization measurements. It is worth mentioning that this condition also ensures that slight errors in the deionization control will have only a marginal effect on the pair interaction, because the counterions provided by the particles themselves by far outnumber any residual electrolyte ions [cf. Eq. (B2)].

In general, the two effective charges, $Z_{\text{eff},\sigma}$ and $Z_{\text{eff},G}$, differ by some 40% [118]. Further, the charges are close to the theoretically expected saturation limit $Z_{\text{eff},i} = \Psi_{\text{eff},i}a/\lambda_B$ with $\lambda_=$0.72 nm being the Bjerrum length, and $\Psi_{\text{eff},i}$ being the slightly surface chemistry dependent effective surface potential measured by different techniques i [108]. We found, that utilizing $Z_{\text{eff},G}$ to localize the observed melting line in the effective temperature-coupling parameter plane of the phase diagram regularly yielded a good agreement of our results with the theoretical predicted location of the melting line [133–139]. By contrast, no agreement was observed when $Z_{\text{eff},\sigma}$ was used [115,119,120,123], i.e., when neglecting many-body effects on the effective charge. We therefore use $Z_{\text{eff},G}$, the particle number density n, and the microion number density n_s as input for calculating the hard-core Yukawa pair interaction energy in the present study:

$$V(r) = \frac{Z_{\text{eff},G}^2 e^2}{4\pi\epsilon}\left(\frac{\exp(\kappa a)}{1+\kappa a}\right)^2 \frac{\exp(\kappa r)}{r}, \tag{B1}$$

with the elementary charge e, the solvent dielectric permittivity $\epsilon = \varepsilon_0\varepsilon_r$, and the screening parameter

$$\kappa = \frac{e^2}{\epsilon k_B T}\sqrt{nZ_{\text{eff},G}z^2 + n_s z^2}, \tag{B2}$$

where $z = 1$ is the microion valency. The microion number density n_s is calculated accounting for ions stemming from added electrolyte (as measured from conductivity) and dissolved CO_2 (using temperature dependent solubilities [140]) as well as ions from the self-dissociation of the solvent ($c = 2 \times 10^{-7}$ mol l^{-1} at pH 7). Note that for the analyzed data, the counterion density which is explicitly accounted for through the $nZ_{\rm eff}$ term in all cases contributes the overwhelming majority of screening ions.

APPENDIX C: DETERMINATION OF CNT-BASED EFFECTIVE NONEQUILIBRIUM IFES FROM NUCLEATION AND GROWTH MEASUREMENTS

To apply CNT for obtaining estimates of the effective nonequilibrium IFEs one needs nucleation rates measured at known metastability. The procedures involved to obtain both rates and the corresponding $\Delta\mu$ values from optical experiments have already been described in the literature ([34,36] and references therein). We here outline both. We start with the growth measurements used to determine $\Delta\mu$ and continue with the nucleation experiments to obtain J. We the proceed with a comparison of CNT-based evaluation schemes to obtain estimates of γ and $\sigma(\Delta\mu)$.

Growth measurements employ microscopy to obtain the growth velocity of crystals. Most suitable contrast variants are Bragg microscopy [62] or polarization microscopy [141]. Both allow direct determination of the crystal extension from the microscopy images. Rectangular flow through cells are used for microscopic investigation. Charged spheres crystallize with bcc structure at low salt and particle concentrations with a narrow coexistence region separating freezing and melting line in a particle number density versus salt concentration phase diagram [34]. Using the conditioning system described above, the suspension is kept in a shear molten state. The flat cell wall acts as the nucleus for a wall crystal which starts growing in the [110] direction immediately after cessation of shear [142]. Just above melting, growth in the [110] direction is slower than the average radial growth, but this difference vanishes for larger metastability [62]. Experiments are best performed at conditions just above melting. Across the coexistence region, a sublinear growth is observed, due to the parallel establishment of the difference in density between both phases. Far above melting, growth occurs over very short times only, as it gets very fast and is quickly stopped upon intersection with bulk nucleated crystals. Just above melting, linear wall crystal growth is observed over sufficiently extended times and lengths. Figure 9 shows typical growth curves. Growth velocities above coexistence (at coexistence) are inferred from the slope (the limiting slope for $t = 0$) of the curves. They first increase with increased metastability but then level off at a plateau. Such behavior is typical for reaction controlled growth and well described by a Wilson-Frenkel growth law:

$$v(\Delta\mu) = v_\infty[1 - \exp(-\Delta\mu/k_BT)] \qquad \text{(C1)}$$

with the limiting velocity v_∞. The crucial point is the use of a suitable approximation for $\Delta\mu$, the chemical potential difference between the two phases. In principle, this quantity depends on the independently measurable interaction parameters effective charge $Z_{\rm eff}$ (from elasticity measurements [118]), particle number density n (from static light scattering [34,143]), and salt concentration c (from conductivity [118,128,129]). In his seminal work, Aastuen *et al.* suggested to use the approximation

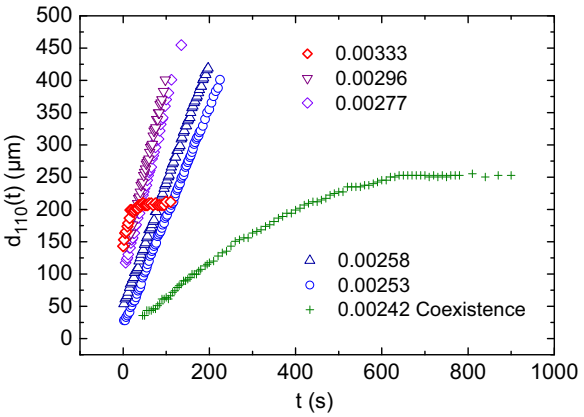

FIG. 9. Typical wall crystal growth curves obtained for different particle volume fractions as indicated.

$$\Delta\mu \simeq B\frac{n - n_F}{n_F}, \qquad \text{(C2)}$$

where F denotes freezing and B is a proportionality constant used as second fit parameter. This approximation neglects any influence of the charge and the salt concentration and any change of the interaction with n. Würth *et al.* [62] therefore suggested using a reduced density difference

$$\Delta\mu \simeq B\Pi^* = B\frac{\Pi - \Pi_F}{\Pi_F} \qquad \text{(C3)}$$

with $\Pi = \alpha n V(d_{NN})$, $V(d_{NN})$ denoting the pair interaction potential at the nearest neighbor distance and α being a coordination number [62]. Since the latter may differ within different phases, one compares the values for the melt to those of the fluid phase at freezing. This exploits that close to a phase transition the Gibbs free energy difference is approximately linear for any pair of phases. Würth's approximations have been thoroughly tested and curves of v versus Π^* measured varying different interaction parameters collapse to a single master curve [34] which is well described by Eq. (C1). It thus accounts for changes in any of the interaction parameters and allows, for instance, measurements in dependence on the salt concentration at fixed n. Typical fit parameter values are $B = 1.5$–15 and $v_\infty = 2$–20 μm/s. Limiting velocities show some scaling with the particle size [34], but there are indications that in addition the thickness of the interfacial region may be of some importance [144].

At the time of the original publication of the nucleation data of PS90, PS100B, and their mixture, no growth data were available. Some time later, these were measured and our results for PS90 are shown in Fig. 10. Note the low velocities across the coexistence region $n_F \leqslant n \leqslant n_M$ with n_M now determined to be $n_M = 4.6$ μm^{-3}. Unfortunately, the salt concentration was not measured accurately enough in these experiments and therefore the fit of the WF law could only be performed using Aastuen's approximation. It returned a value of $B_{PS90} = 4 \pm 0.6$ for the proportionality constant and

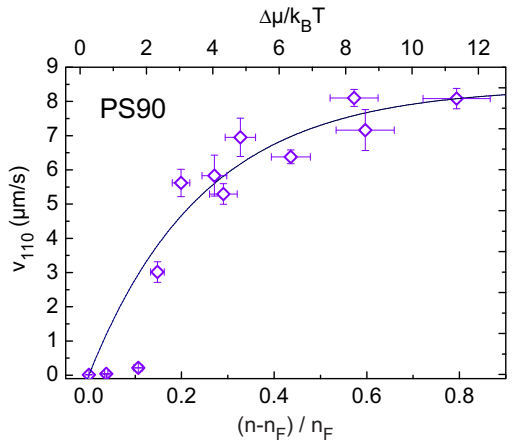

FIG. 10. Growth velocities of PS90 in dependence on the reduced density. The solid line is a fit using Eq. (C1) with Eq. (C2). The fit parameters obtained are $B_{PS90} = 4 \pm 0.6$ for the proportionality constant and $v_\infty = 8.4 \pm 0.3$ μm/s for the limiting velocity.

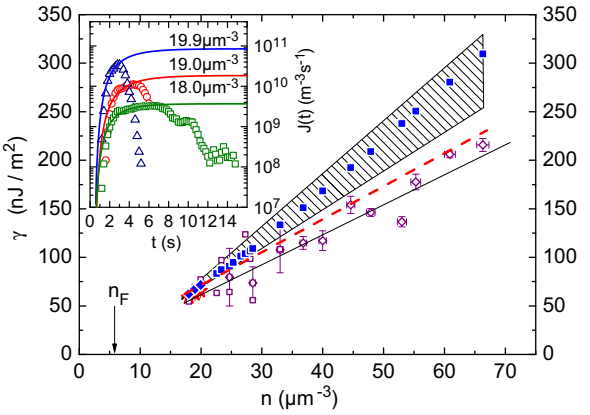

FIG. 11. Density dependence of the interfacial free energies γ of PnBAPS68 obtained from different evaluation schemes. Solid symbols denote use of CNT with J_0 calculated using Eq. (C6) in Eq. (C5) with $A = 1$ and $D_{\text{eff}} = 0.1 D_0$ and different input data: average nucleation rate density J_{AVR} (squares), maximum nucleation rate density J_{MAX} (diamonds), or steady state nucleation rate density J_{SS} (stars); hatched area denotes the maximum systematic change by setting $D_{\text{eff}} = D_0$ (upper bound) or $D_{\text{eff}} = 10^{-3} D_0$ (lower bound). Open symbols denote data from two different experimental runs using a corrected version graphical evaluation [146]. The solid line gives a least-square linear fit to these data. The dashed red line gives the $\gamma(n)$ values obtained from the fit of Eq. (C8) to the data as shown in Fig. 12. All curves increase linearly with n for $n > n_F$. Inset: time dependent nucleation rate densities for three densities n as indicated. With increased n, transient effects become more pronounced. Solid lines are the fits of Kashchiev's theory yielding J_{SS} [60].

$v_\infty = 8.4 \pm 0.3$ μm/s for the limiting velocity. The growth data for PS100B were measured by Liu *et al.* [145] with simultaneously determined salt concentrations. Evaluation using Aastuen's (Würth's) approximation yielded $B = 4.0 \pm 0.3$ ($B = 2.6 \pm 0.2$). For the present paper, we decided to use the value from Aastuen's approximation, which allowed us to adopt an estimate of $B = 4.0$ for the mixture as well. The new values for $\Delta\mu$ were used to re-evaluate the nucleation experiments and obtain estimates for the IFE. The corrected values of the IFEs differ only slightly from the original ones, but their increase with increasing $\Delta\mu$ was found to be much stronger due to the use of the smaller proportionality constant.

Measurements of the nucleation rates were performed by microscopy [54], static light scattering, or time resolved USAXS measurements [11,30,119]. Direct video microscopy could be applied at low metastability, where nucleation sites are sufficiently distant to be resolved and nucleation rates are small enough to be followed (typically well below 10^2 s^{-1}). Rates were divided by a suitable expression for the free volume. The original Avrami model considers bulk nucleating crystals only, assuming their sites to be Poisson distributed and their nucleation rate density being constant in time [57]. It was extended by Wette *et al.* [54] to also include competing wall crystal growth and variable rates. The resulting expression for the relative free volume at time t reads

$$F(t) = \frac{(V_0 - 2Ad_0 - 2Av_W t)}{(V_0 - 2Ad_0)} \exp\left(-\frac{4\pi}{3} \times \sum_i \frac{m_i}{V_0 - 2Ad_0 - 2Av_W\tau_i}[R_0 + v(t-\tau_i)^3]\right), \quad \text{(C4)}$$

where V_0 is the total observed volume, A, d_0, and v_W are, respectively, the observed area, initial thickness, and growth velocity of the wall crystal. m_i is the number of crystallites appearing at times $\tau_i = i\,\Delta t$ with Δt typically on the order of a few tenths of a second. R_0 and v are the bulk crystallite radius at first identification and its growth velocity, respectively.

An example of resulting nucleation rate densities obtained for PnBAPS68 is semilogarithmically plotted in the inset of Fig. 11. After a short induction time, $J(t)$ first increased sharply, then settled to a plateau, before decreasing again. With increasing n the plateau extension shrank and the maximum values increased considerably. Close to the phase boundary, the nucleation rate density stayed constant over an extended time and therefore the steady state nucleation rate density J_{SS}, required by CNT, was well approximated by the plateau value J_{MAX}. At larger n data were fitted by Kashchiev's theory of transient nucleation [60]. This is also shown in the inset of Fig. 11. Note the increased value at long times, which is identified to J_{SS} and becomes larger than J_{MAX} for number densities $n > 10^{19}$ m^{-3} s^{-1}.

At larger rates, postsolidification images of the sample were taken. The distributions of probability density for the radially averaged linear dimension of crystallites, L, are obtained by image analysis. Typical distributions were slightly skewed to large L values and well described by a log-normal distribution. With increasing n, the average crystallite size shifted to smaller values. Since here the wall crystal correction to $F(t)$ was negligible, the original Avrami formula was used. It connects the crystallite density and growth velocity to an average nucleation rate density as $J_{AVR} = (1/\alpha) v \rho^{4/3}$. Here, $1/\alpha = 1.158$ is a geometrical factor. $\rho \equiv \langle L \rangle^{-3}$ is the crystallite density and $\langle L \rangle$ is the average linear dimension of crystallites assumed to be cube shaped.

At still larger rate densities, the crystallites became too small to be properly resolved by microscopy. Then scattering methods were applied. Here, raw data $I(q,t)$ were first desmeared [11,30] to isolate the scattering signal from apparative contributions. For isolating the crystal structure factor in the time-resolved USAXS measurements, the fluid background (obtained from the first measurement immediately after shear melting) was subtracted with a weighting factor β denoting the fraction of remaining melt. We then divided the signal by the independently measured form factor $P(q)$. The isolated crystal structure factor $S_X(q,t)$ showed Bragg peaks which grew and sharpened over time. Further evaluation followed Harland *et al.* [29] to obtain (i) the crystallinity (fraction of crystallized material) $X(t)$ from the integrated intensity normalized to the long time value after complete solidification, (ii) the average linear dimension $\langle L\rangle$ of crystallites from the peak width, and (iii) their number density $\rho(t)$ from dividing $X(t)$ by the average volume of crystals. From the derivatives of the average linear dimension and the number density we obtained the growth velocity and the time dependent nucleation rate density $J(t)$. Like for the microscopy data, the time dependent nucleation rate densities could be fitted by Kashchiev's expression for transient nucleation to return J_{SS}.

In light scattering experiments, no time dependent data were measured. Rather, a postsolidification analysis was performed, using the average linear dimension $\langle L\rangle$ from the width of the observed Bragg peaks, the limiting velocity from the growth experiments and Avrami's formula to calculate J_{AVR}. We note that the light scattering data may be biased by the presence of a finite and presumably skewed crystallite size distribution. Neglect of this influence in our analysis may, in principle, lead to inconsistencies between the nucleation rates determined by this technique and by the direct size distribution analysis performed at intermediate n. In fact, the change of slope in Fig. 12 occurs close to the range in which the data taken by the different techniques overlap. It thus could indicate such an inconsistency. However, this change of slope is systematically present also in Fig. 13. There, the data taken for the other CS samples were taken by light scattering only. Therefore, the good agreement between the data derived from different techniques as displayed in Fig. 12 suggests that a finite crystallite size distribution hardly influences the data evaluation and even less the conclusions drawn in this paper.

PnBAPS68 has been measured using all outlined optical techniques, except USAXS [30,54,122]. In [55] we have compared these to find an excellent agreement between the nucleation rate densities obtained by the different methods. This is also seen in Fig. 12 which shows the nucleation rate densities measured with different methods for $n =$ 18–67 μm^{-3}. The data cover several orders of magnitude in J without any systematic deviation between the different data sets. Similar data are displayed for a collection of different colloidal species also in Fig. 13. Here, we plotted J versus the volume fraction, $\Phi = \frac{n(4\pi/3)a^3}{V_0}$, to once more stress the non-space-filling character of CS crystals in comparison to HSs, which crystallize above $\Phi_M = 0.495$ [147]. Note the characteristic shape of all CS curves. The nucleation rate density increases by several orders of magnitude for small changes in Φ. The increase is more pronounced at smaller

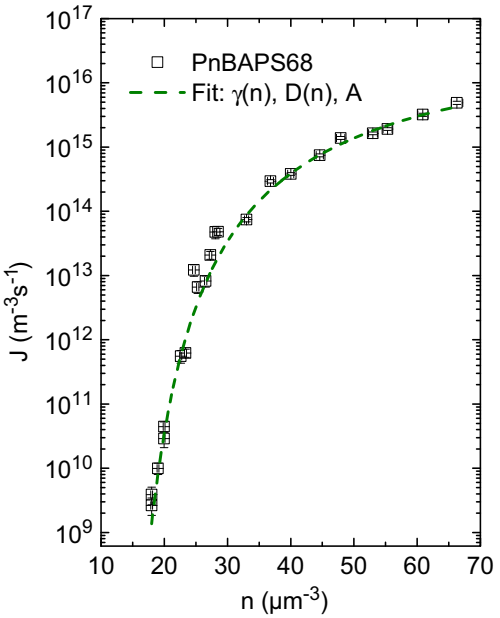

FIG. 12. Nucleation rate densities of PnBAPS68 as measured by video microscopy ($n = 18$–19.9 μm^{-3}), postsolidification crystal size analysis ($n = 18$–33 μm^{-3}), and static light scattering ($n =$ 25–67 μm^{-3}). Note the excellent agreement between data derived from different methods. The solid line is a least-square fit of Eq. (C8) to the data using A, $D_L^S(n)$, and $\gamma(n)$ as free parameters. An excellent description of the experimental data can be observed. The obtained $\gamma(n)$ are shown in Fig. 11 as a dashed red line.

Φ. By contrast, the HS data display a maximum, which is attributed to the vanishing long time self-diffusion upon approaching the HS glass transition at $\Phi_G = 0.57$–0.59 [34].

While different techniques to obtain nucleation rate densities yield consistent results, systematic differences are introduced in the next step of evaluation. Several CNT-based schemes exist. CNT in its simplest form assumes that the

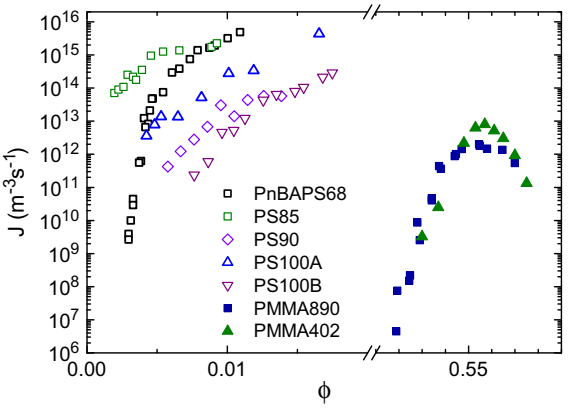

FIG. 13. Nucleation rate densities of different colloidal species vs volume fraction. Open symbols denote charged sphere systems with their diameters indicated. Closed symbols refer to data obtained for two HS systems (PMMA890: [34]; PMMA402: [29]. Note the low volume fractions of CS and the steepness of the increase in J

steady state nucleation rate density is given by

$$J_{SS} = J_0 \exp(-\Delta G^*/k_B T), \tag{C5}$$

where for colloidal systems the nucleation barrier $G^* = 16\pi\gamma^3/3(n\Delta\mu)^2$ is determined by the IFE γ, the difference in chemical potential $\Delta\mu$, between the melt and the solid phase, and the particle number density n. J_0 is a kinetic prefactor which for colloids with diffusive dynamics and particle by particle attachment was proposed to be [34,148]

$$J_0 = An\frac{D_L^S}{\ell^2} \tag{C6}$$

where D_L^S is the long-time self-diffusion coefficient, A is a dimensionless factor, and ℓ is a characteristic length scale approximated by $\ell = d_{NN} \approx n^{-1/3}$. In most publications, the dimensionless factor A has been set to unity as a first approximation.

Use of Eq. (C6) in Eq. (C5) to calculate γ affords an additional assumption about the n dependence of D_L^S. For charged spheres showing no glass transition in the range of investigated n, D_L^S is limited as $D_0 \geqslant D_L^S \geqslant 10^{-3}D_0$, where the upper bound is the Stokes-Einstein diffusion coefficient $D_0 = k_B T/6\pi\eta a$ and the lower bound is estimated from the results of published diffusion data on charged spheres [149]. For the calculation of the data points in Fig. 11, we used the approximation $D_L^S = 0.1D_0$ which corresponds to applying Löwen's dynamical freezing criterion [150] to estimate the diffusivity at freezing and neglecting the (weak) density dependence over the volume fraction range investigated. The hatched area denotes the maximum systematic change by varying D_{eff} within the mentioned bounds.

Alternatively, a graphical evaluation from a plot of $\ln(J)$ versus $1/(n\Delta\mu)^2$ was performed [55]. The slope of this curve is $m = 16\pi\gamma(n)^3/k_B T$. The results of this graphical evaluation are also shown in Fig. 11. They appear to lie systematically below the results of other evaluation schemes. Further, the noise in the $J(n)$ data directly translates into a noticeable scatter of $\gamma(n)$. However, the linear increase with increasing n is clearly seen despite this scatter. Note that the graphical evaluation does not make any assumptions about the kinetic prefactor. Thus, the results shown in Fig. 11 demonstrate the pronounced metastability dependence of γ.

Further, an explicit calculation of the kinetic prefactor within the framework of CNT following [40] was performed in [55] to yield

$$J_{0,CNT} = 12\left(\frac{4}{3}\right)^{2/3}\pi^{-1/3}n^{4/3}\sqrt{\frac{\gamma}{k_B T}}D_L^S. \tag{C7}$$

In comparison to Eq. (C6), this prefactor has a differing n dependence and further depends on an n-dependent nonequilibrium IFE. In [55], this approach was used to obtain estimates for both the nonequilibrium IFE and the kinetic prefactor. Interestingly, no acceptable fit could be obtained using Eq. (C7) directly in Eq. (C5). Therefore the authors performed a least-square fit to the n-dependent measured nucleation rate densities using

$$J_{SS} = An^{4/3}\sqrt{\frac{\gamma}{k_B T}}D_L^S \exp\left(\frac{-16\pi\gamma^3}{3k_B T(n\Delta\mu)^2}\right). \tag{C8}$$

Here, a constant A, a variable surface tension $\gamma(n)$, and a variable self-diffusion constant $D_L^S(n)$ were used as fitting parameters. As shown in Fig. 12, an excellent fit can be obtained. Further, the results of this fit can be described in terms of second order polynomials $\gamma(n) = (b_0 + b_1 n + b_2 n^2)$ and $D_L^S(n) = (a_0 + a_1 n + a_2 n^2)D_0$. The polynomial for $\gamma(n)$ is shown in Fig. 11 as a dashed red line lying between the results of the other two methods of evaluation.

Taking the reduced values and applying our extrapolation scheme to each, the differently obtained $\gamma(n)$ in Fig. 11 yield estimates for the equilibrium IFE differing by less than 5%. Slopes and thus Turnbull coefficients differ by approximately 10%. Even though these differences are small, the results from graphical evaluation appear to be at systematically lower values, while the results from fits of Eqs. (C5) and (C6) using $D_L^S = 0.1D_0$ systematically show larger values than those obtained via fits of Eq. (C8). Therefore, $\sigma(n)$ for all latex spheres compiled in Fig. 1 data were based on γ derived via fits of Eq. (C8).

An equally satisfying agreement is not observed for the kinetic prefactors obtained from the three different evaluation schemes. This was shown in [55], too. Using the graphical evaluation, the kinetic prefactor J_0,graph(n) was obtained from extrapolating the locally fitted slope to $1/(n\Delta\mu)^2 = 0$ corresponding to infinite metastability. Using Eq. (C5) in Eq. (C6) with $A = 1$ results in a prefactor $J_{0,\text{approx}}(n)$. Finally, $D_L^S(n)$ and $\gamma(n)$ from the fit of Eq. (C8) were used in Eq. (C7) to calculate the n-dependent kinetic preactor $J_{0,CNT}(n)$ in a point-by-point manner. The results for these prefactors differed considerably. Compared to the measured $J(n)$, $J_{0,\text{graph}}(n)$ showed a somewhat less pronounced n dependence and up to two orders of magnitude larger values. The difference was getting smaller with increasing n. The n dependence of both other sets of prefactors was by far weaker. I.e., in both curves, an increase of $J_0(n)$ of about one order of magnitude over the complete investigated range of n was observed. However, $J_{0,\text{approx}}(n)$ was found to be up to seven orders of magnitude larger than measured $J(n)$ and $J_{0,CNT}(n)$ was found to be up to 12 orders of magnitude larger than $J(n)$. Thus far, no good reason has been proposed as to why the kinetic prefactors show such large discrepancies, while the IFEs appear to be rather insensitive to the choice of the evaluation scheme.

APPENDIX D: USE OF CNT AND RELATED SCHEMES TO OBTAIN NONEQUILIBRIUM IFES

CNT provides a simple model for nucleation kinetics in first order transitions [37–41]. The model is based on the idea that nucleation is an activated process and hence contains a Boltzmann factor with an energy barrier ΔG^*. Further, a kinetic prefactor limits the reaction rate. Expressions for this prefactor have been worked out assuming particle-by-particle attachment. CNT was originally proposed to describe vapor condensation. Therefore, in most versions of CNT (including those used for melt crystallization), it is further assumed that the nuclei are spherical. This, in turn, implies that the barrier can be written in terms of surface energy loss and volume energy gain based on a single geometrical parameter only, the nucleus radius r. CNT is generally believed to capture the basic physics of homogeneous nucleation. However, the

justification of many of the made assumptions is still discussed controversially. Therefore, the desire for a comprehensive microscopic theory remains urgent.

CNT allows simple predictions that only require a few (measurable) bulk thermodynamic data. Its predictive success, however, has been shown to be quite limited. Deviations in estimated and measured nucleation rate densities of up to 35 orders of magnitude occur for melt crystallization of metals as well as for vapor condensation and also in colloidal HS systems [36,63,151–153]. Also other measured quantities deviate strongly from predictions [154]. This has been blamed on a number of issues, both conceptually and practically. Finding workarounds or solutions has become a field of great interest [151,155].

The most obvious conceptual criticism aims at the use of a macroscopic concept, the IFE, on the scale of clusters and the application of equilibrium values of thermodynamic quantities under nonequilibrium conditions. In fact, CNT takes a macroscopic continuum view and describes clusters of discrete particles as small, noninteracting chunks of thermodynamically well defined new bulk phases separated from unchanged, isotropic, and homogeneous background melt. Discreteness enters only through growth by addition of individual particles. This view implies a number of consequences. For example, CNT assumes nuclei with sharp interfaces. As already early simulation work has revealed [156,157], this capillarity approximation is hardly ever met on the molecular scale. Like for equilibrated, flat interfaces, density functional theory and explicitly microscopic models of the interface have therefore been used to meet this challenge [92,155]. In addition, in CNT, nuclei are often assumed to be spherical. Typically, this is an oversimplification, as both computer studies and experiments on metals or colloids show [16,27,91]. Based on Walton's atomic nucleation theory (ANT) [158] and other approaches, several variants have been developed to include nonspherical shapes into the CNT scheme or presenting corrected CNT formulas [159]. Alternatively, the spherical shape was kept and a curvature and thus size dependent IFE was introduced [160,161]. Both attempt to describe the very small nuclei encountered at large metastability. Under conditions of large metastability, another issue is encountered, because due to its construction CNT and extensions do not allow for a description of spinodal processes [162]. Here, a workaround may be seen in the kinetic model of Dixit and Zukoski [163] which in fact yields a good description of the HS nucleation rates down to volume fractions close to freezing.

Furthermore, there are several practical issues. Again, some are concerned with the nucleus shape and size. Scattering experiments typically determine orientationally averaged data referring to an effective sphere of equivalent size. Microscopy reveals irregular and nonspherical forms but often lacks the statistics needed to obtain thermodynamically meaningful averages. Further, the assumption of spatial and temporal homogeneity in terms of pressure, temperature, and concentration of monomers may not be met, i.e., in experiments very often it cannot be assured that conditions stay that way throughout the complete crystallization process [164]. This affords additional theoretical efforts [60,165,166]. In addition, at large metastability, interactions between neighboring nuclei may occur leading to jamming or coalescence [12] and two-step nucleation may be an important alternative mechanism [24,167,168]. Finally, issues of constrained volume may play a role in both experiment and simulations [169].

In view of all these issues, the mediocre performance of CNT and its derivatives in *predicting* nucleation rate densities, critical nucleus sizes, or onset of nucleation with decreasing temperature or increasing pressure is not very surprising. As discussed above, this is also observed in the data on PnBAPS68. Using Eq. (C7) in Eq. (C5) no acceptable two parameter fit to the nucleation rate densities of PnBAPS68 could be obtained. Further, the prefactors calculated using Eq. (C7) with the results of the very good fit of Eq. (8) to the data shown in Fig. 12 appeared to be unreliably large values.

However, in the present paper and the ones providing the original IFE data, CNT was used differently. In fact, it was only utilized to parametrize nucleation kinetic data and to obtain estimates of the nonequilibrium IFE as a function of system metastability. This use of CNT is much less ambitious and is by far less challenged by the aforementioned issues. For instance, the extended experiments on PnBAPS68 using several different techniques ranging from direct counting to postsolidification analysis employing Avrami theory yielded consistent nucleation rate densities with $J(n)$ overlapping over more than an order of magnitude in J. As seen in Fig. 13, these data are representative for a large number of CS systems and covers nucleation rate densities over many orders of magnitude. Three different CNT-based methods of extracting IFEs were employed. The graphical evaluation results are of particular importance. As can be seen in Fig. 11 the effective IFEs assemble within statistical uncertainty on a straight line which demonstrates the linear dependence of the nonequilibrium IFE on the degree of metastability. Since this result was obtained without making any assumption on the kinetic prefactor it lays the basis for the validity of the extrapolation procedure employed in the main part of this paper. The same trend is seen for the data derived using Eq. (C6) which neglects the γ dependence of the prefactor altogether and the IFEs derived from the fit by Eq. (C8), where it was accounted for without explicitly calculating A. The comparison in Fig. 11 therefore shows that all three procedures capture the IFE dependence of the barrier qualitatively correctly. The spread in extrapolated equilibrium IFEs due to the use of different evaluation procedures amounts to some five percent which is on the same order as the statistical uncertainty. The spread in slopes is somewhat larger but still acceptable.

Two more points deserve further attention. The first is the low absolute values of the IFE of a few hundred $\mathrm{nJ/m^{-2}}$ as compared to, e.g., metals, where typically values of about $250\ \mathrm{mJ/m^{-2}}$ are obtained [43,91]. This is due to the low number density of colloidal suspensions and has the important consequence that colloidal crystal nuclei have fuzzy shapes [16,17], while metal crystal nuclei appear to be much more compact [91]. The reduced values for the CS IFE compared in Fig. 6, however, are only an order of magnitude lower than the reduced metal IFEs. Second, The different treatment of the CNT-predicted $\gamma^{1/2}$ dependence of J_0 in the three evaluation schemes results in systematic quantitative differences in the derived $\gamma(n)$. We here opted for using a fit procedure for all latex systems, because it incorporates

the full CNT-predicted IFE dependence of J, had the least statistical and/or systematic uncertainties, and shows values midway between those resulting from the alternative schemes. The obtained values are therefore understood as CNT based effective nonequilibrium estimates of the IFE.

In the main part of the paper we extrapolated these data to zero metastability. This effort is not backed by CNT itself. Rather it is suggested by the linear dependence of γ on n, respectively the linear dependence of σ on $\Delta\mu$ up to largest metastabilities as seen in Fig. 1. We note that for PnBAPS68 the radius of the critical nucleus varied over the investigated range between one and several d_{NN} [55]. The other species had been investigated at even larger metastability. The observed strictly linear dependence of σ on $\Delta\mu$ thus appears to exclude any dependence of σ on the size of the critical nucleus. A linear dependence of the nonequilibrium IFE on metastability has been observed before in many systems and was extensively discussed, e.g., by Jiang [43]. Moreover, in HSs, the volume fraction dependent CNT-based estimates of the nonequilibrium IFE linearly decrease with decreasing volume fraction to meet the theoretical and experimental values of the equilibrium IFE at the freezing volume fraction [24]. Our present extrapolation returned effective equilibrium IFE values between those of HSs and those of metals. It remains to be seen whether future simulations or measurements of the macroscopic IFE of colloidal CS with explicit micro-ions will coincide.

[1] D. J. Wales and H. A. Scheraga, Global Optimization of Clusters, Crystals, and Biomolecules, Science **285**, 1368 (1999).

[2] F. Baletto and R. Ferrando, Structural properties of nanoclusters: Energetic, thermodynamic, and kinetic effects, Rev. Mod. Phys. **77**, 371 (2005).

[3] S. C. Glotzer and M. J. Solomon, Anisotropy of building blocks and their assembly into complex structures, Nat. Mater. **6**, 557 (2007).

[4] A. Malins, S. R. Williams, J. Eggers, H. Tanaka, and C. P. Royall, Geometric frustration in small colloidal clusters, J. Phys.: Condens. Matter **21**, 425103 (2009).

[5] F. Li, D. P. Josephson, and A. Stein, Colloidal Assembly: The Road from Particles to Colloidal Molecules and Crystals, Angew. Chem. Int. Ed. **50**, 360 (2011).

[6] F. Calvo, J. P. K. Doye, and D. J. Wales, Energy landscapes of colloidal clusters: thermodynamics and rearrangement mechanisms, Nanoscale **4**, 1085 (2012).

[7] D. J. Kraft, R. Wittkowski, B. ten Hagen, K. V. Edmond, D. J. Pine, and H. Löwen, Brownian motion and the hydrodynamic friction tensor for colloidal particles of complex shape, Phys. Rev. E **88**, 050301(R) (2013).

[8] P. Lu and D. A. Weitz, Colloidal Particles: Crystals, Glasses, and Gels, Annu. Rev. Condens. Matter Phys. **4**, 217 (2013).

[9] C. Weis, I. Natalia, and N. Willenbacher, Effect of weak attractive interactions on flow behavior of highly concentrated crystalline suspensions, J. Rheol. **58**, 1583 (2014).

[10] H. J. Schöpe, G. Bryant, and W. van Megen, Two Step Crystallization Kinetics in Colloidal Hard Spheres, Phys. Rev. Lett. **96**, 175701 (2006).

[11] D. M. Herlach, I. Klassen, P. Wette, and D. Holland Moritz, Colloids as model systems for metals and alloys: A case study of crystallization, J. Phys.: Condens. Matter **22**, 153101 (2010).

[12] H. J. Schöpe and T. Palberg, Frustration of structural fluctuations upon equilibration of shear melts, J. Non-Cryst. Solids **307-310**, 613 (2002).

[13] P. R. ten Wolde and D. Frenkel, Enhancement of protein crystal nucleation by critical density fluctuations, Science **277**, 1975 (1997).

[14] U. Gasser, A. Schofield, and D. A. Weitz, Local order in a supercooled colloidal fluid observed by confocal microscopy, J. Phys.: Condens. Matter **15**, S375 (2003).

[15] J. F. Lutsko and G. Nicolis, Theoretical Evidence for a Dense Fluid Precursor to Crystallization, Phys. Rev. Lett. **96**, 046102 (2006).

[16] P. Tan, N. Xu, and L. Xu, Visualizing kinetic pathways of homogeneous nucleation in colloidal crystallization, Nat. Phys. **10**, 73 (2014).

[17] K. Kratzer and A. Arnold, Two-stage crystallization of charged colloids under low supersaturation conditions, Soft Matter **11**, 2174 (2015).

[18] P. R. tenWolde, M. J. Ruiz-Montero, and D. Frenkel, Numerical Evidence for bcc Ordering at the Surface of a Critical fcc Nucleus, Phys. Rev. Lett. **75**, 2714 (1995).

[19] D. Moroni, P. R. ten Wolde, and P. G. Bolhuis, Interplay Between Structure and Size in a Critical Crystal Nucleus, Phys. Rev. Lett. **94**, 235703 (2005).

[20] J. Russo and H. Tanaka, The microscopic pathway to crystallization in undercooled fluids, Sci. Rep. **2**, 505 (2012).

[21] J. Russo and H. Tanaka, Selection mechanism of polymorphs in the crystal nucleation of the Gaussian core model, Soft Matter **8**, 4206 (2012).

[22] G. Tarjus, S. A. Kivelson, Z. Nussinov, and P. Viot, The frustration-based approach of supercooled liquids and the glass transition: a review and critical assessment, J. Phys.: Condens. Matter **17**, R1143 (2005).

[23] C. P. Royall, S. R. Williams, T. Ohtsuka, and H. Tanaka, Direct observation of a local structural mechanism for dynamic arrest, Nat. Mater. **7**, 556 (2008).

[24] M. Franke, S. Golde, and H. J. Schöpe, Solidification of a colloidal hard sphere like model system approaching and crossing the glass transition, Soft Matter **10**, 5380 (2014).

[25] J. D. Bernal, J. Mason, and K. R. Knight, Radial Distribution of the Random Close Packing of Equal Spheres, Nature (London) **194**, 957 (1962).

[26] A. V. Anikeenko and N. N. Medvedev, Polytetrahedral Nature of the Dense Disordered Packings of Hard Spheres, Phys. Rev. Lett. **98**, 235504 (2007).

[27] T. Schilling, H. J. Schöpe, M. Oettel, G. Opletal, and I. Snook, Precursor-Mediated Crystallization Process in Suspensions of Hard Spheres, Phys. Rev. Lett. **105**, 025701 (2010).

[28] T. Kawasaki and H. Tanaka, Formation of a crystal nucleus from liquid, Proc. Natl. Acad. Sci. USA **107**, 14036 (2010); **108**, 6335 (2011).

[29] J. L. Harland and W. van Megen, Crystallization kinetics of suspensions of hard colloidal spheres, Phys. Rev. E **55**, 3054 (1997).

[30] P. Wette, H. J. Schöpe, J. Liu, and T. Palberg, Solidification in model systems of spherical particles with density dependent interaction, Europhys. Lett. **64**, 124 (2003).

[31] P. Wette, H. J. Schöpe, and T. Palberg, Crystallization in charged two component suspensions, J. Chem. Phys. **122**, 144901 (2005).

[32] A. Kozina, P. Diaz-Leyva, E. Bartsch, and T. Palberg, Crystallization kinetics of colloidal binary mixtures with depletion attraction, Soft Matter **10**, 9523 (2014).

[33] D. M. Herlach, Colloids as model systems for metals and alloys: a case study of crystallization, Eur. Phys. J.: Spec. Top. **223**, 591 (2014).

[34] T. Palberg, Crystallisation kinetics of repulsive colloidal spheres, J. Phys.: Condens. Matter **11**, R323 (1999).

[35] U. Gasser, Crystallization in three- and two-dimensional colloidal suspensions, J. Phys.: Condens. Matter **21**, 203101 (2009).

[36] T. Palberg, Crystallization kinetics of colloidal model suspensions: recent achievements and new perspectives, J. Phys.: Condens. Matter **26**, 333101 (2014).

[37] M. Volmer and A. Weber, Z. Phys. Chem. **119**, 227 (1926).

[38] R. Kaischew and I. N. Stranski, On the kinetic deflection rate of germ formation, Z. Phys. Chem. Abt. B **26**, 317 (1934).

[39] R. Becker and W. Döring, Kinetische Behandlung der Keimbildung in übersättigten Dämpfen, Ann. Phys. **416**, 719 (1935).

[40] J. Zeldovich, A theory of the ignition on incandescent surfaces, J. Exp. Theor. Phys. **12**, 525 (1942).

[41] D. Turnbull and J. C. Fisher, Rate of nucleation in condensed systems, J. Chem. Phys. **17**, 71 (1949).

[42] J. F. Lutsko, A dynamical theory of nucleation for colloids and macromolecules, J. Chem. Phys. **136**, 034509 (2012).

[43] Q. Jiang and H. M. Lu, Size dependent interface energy and its applications, Surf. Sci. Rep. **63**, 427 (2008).

[44] J. Antonowicz, E. Jezierska, M. Kedzierski, A. R. Yavari, L. Greer, P. Panine, and M. Sztucki, Early stages of phase separation and nanocrystallization in Al-rare earth metallic glasses studying using SAXS/WAXS and HRTEM methods, Rev. Adv. Mater. Sci. **18**, 454 (2008).

[45] M. Asta, F. Spaepen, and J. F. van der Veen (Guest Editors), Solid-Liquid Interfaces: Molecular Structure, Thermodynamics, and Crystallization, MRS Bull. **29**, 920 (2004).

[46] K. F. Kelton, Crystal nucleation in liquids and glasses, Solid State Phys. **45**, 75 (1991).

[47] W. Ostwald, Studien uber die Bildung und Umwandlung fester Körper, Z. Phys. Chem. **22**, 289 (1897).

[48] S. Alexander and J. P. McTague, Should All Crystals Be bcc? Landau Theory of Solidification and Crystal Nucleation, Phys. Rev. Lett. **41**, 702 (1978).

[49] N. V. Dziomkina and G. J. Vancso, Colloidal crystal assembly on topologically patterned templates, Soft Matter **1**, 265 (2005).

[50] T. Gorishnyy, C. K. Ullal, M. Maldovan, G. Fytas, and E. L. Thomas, Hypersonic Phononic Crystals, Phys. Rev. Lett. **94**, 115501 (2005).

[51] R. P. Sear, Nucleation: theory and applications to protein solutions and colloidal suspensions, J. Phys.: Condens. Matter **19**, 033101 (2007).

[52] D. Turnbull, Formation of crystal nuclei in liquid metals, J. Appl. Phys. **21**, 1022 (1950).

[53] B. B. Laird, The solid-liquid interfacial free energy of close-packed metals: Hard-spheres and the Turnbull coefficient, J. Chem. Phys. **115**, 2887 (2001).

[54] P. Wette, H. J. Schöpe, and T. Palberg, Microscopic investigations of homogeneous nucleation in charged sphere suspensions, J. Chem. Phys. **123**, 174902 (2005).

[55] P. Wette and H. J. Schöpe, Nucletion kinetics of deionized charge colloidal model suspensions: A quantitative analysis by means of classical nucleation theory, Phys. Rev. E **75**, 051405 (2007).

[56] H. J. Schöpe, A. Engelbrecht, and R. Meneses, Heterogeneous and homogeneous crystal nucleation in a colloidal model system of charged spheres at low metastabilities, Soft Matter **7**, 5685 (2011).

[57] A. N. Kolmogorov, Izv. Akad. Nauk SSR Ser. Fiz. Mat. Nauk. 1937, pp. 355–360 (in Russian). An English translation of this work can be found in *Selected Works of A. N. Kolmogorov, Vol. II, Probability Theory and Mathematical Statistics*, edited by A. N. Shiryayev, translated from the Russian by G. Lindquist (Kluwer Academic, Dordecht, 1992), p. 188; W. A. Johnson and R. F. Mehl, Reaction kinetics in processes of nucleation and growth, Trans. A. I. M. M. E. **135**, 416 (1939) (Transactions of the American Institute of Mining, Metallurgical, and Petroleum Engineers, Inc.), available online in K. Barmak, Metallurg. Mater. Trans. A **41**, 2711 (2010): A commentary on reaction kinetics in processes of nucleation and growth, doi:10.1007/s11663-010-9421-1); M. Avrami, Kinetics of phase change. I. General theory, J. Chem. Phys. **7**, 1103, (1939); Kinetics of phase change. II. Transformation-time relations for random distribution of nuclei, *ibid.* **8**, 212, (1940); Kinetics of phase change. III. Granulation, phase change and microstructures, *ibid.* **9**, 177 (1941).

[58] M. Tomellini and M. Fanfoni, Beyond the constraints underlying Kolmogorov-Johnson-Mehl-Avrami theory related to the growth laws, Phys. Rev. E **85**, 021606 (2012).

[59] C. D. Van Siclen, Random nucleation and growth kinetics, Phys. Rev. B **54**, 11845 (1996).

[60] D. Kashchiev, Solution of the non-steady state problem in nucleation kinetics, Surf. Sci. **14**, 209 (1969).

[61] D. J. W. Aastuen, N. A. Clark, L. K. Cotter, and B. J. Ackerson, Nucleation and Growth of Colloidal Crystals, Phys. Rev. Lett. **57**, 1733 (1986); Erratum: Nucleation and Growth of Colloidal Crystals, *ibid.* **57**, 2772(E) (1986).

[62] M. Würth, J. Schwarz, F. Culis, P. Leiderer, and T. Palberg, Growth kinetics of body centered cubic colloidal crystals, Phys. Rev. E **52**, 6415 (1995).

[63] S. Auer and D. Frenkel, Prediction of absolute crystal-nucleation rate in hard-sphere colloids, Nature (London) **409**, 1020 (2001).

[64] A. Härtel, M. Oettel, R. E. Rozas, S. U. Egelhaaf, J. Horbach, and H. Löwen, Tension and Stiffness of the Hard Sphere Crystal-Fluid Interface, Phys. Rev. Lett. **108**, 226101 (2012).

[65] S. Auer and D. Frenkel, Crystallization of weakly charged spheres: a numerical study, J. Phys.: Condens. Matter **14**, 7667 (2002).

[66] T. Zykova-Timan, J. Horbach, and K. Binder, Monte Carlo simulations of the solid-liquid transition in hard spheres and colloid-polymer mixtures, J. Chem. Phys. **133**, 014705 (2010).
[67] Y. Monovoukas and A. P. Gast, The experimental phase diagramm of charged colloidal suspensions, J. Colloid Interface Sci. **128**, 533 (1989).
[68] R. L. Davidchack and B. B. Laird, Direct Calculation of the Crystal-Melt Interfacial Free Energy via Molecular Dynamics Computer Simulation, J. Phys. Chem. B **109**, 17802 (2005).
[69] Y. Mu, A. Houk, and X. Song, Anisotropic Interfacial Free Energies of the Hard-Sphere Crystal-Melt Interfaces, J. Phys. Chem. B **109**, 6500 (2005).
[70] R. L. Davidchack, J. R. Morris, and B. B. Laird, The anisotropic hard-sphere crystal-melt interfacial free energy from fluctuations, J. Chem. Phys. **125**, 094710 (2006).
[71] M. Amini and B. B. Laird, Crystal-melt interfacial free energy of binary hard spheres from capillary fluctuations, Phys. Rev. B **78**, 144112 (2008).
[72] R. L. Davidchack, Hard spheres revisited: Accurate calculation of the solid-liquid interfacial free energy, J. Chem. Phys. **133**, 234701 (2010).
[73] L. A. Fernandez, V. Martin-Mayor, B. Seoane, and P. Verrocchio, Equilibrium Fluid-Solid Coexistence of Hard Spheres, Phys. Rev. Lett. **108**, 165701 (2012).
[74] R. L. Davidchack and B. B. Laird, Direct calculation of the crystal-melt interfacial free energies for continuous potentials: Application to the Lennard-Jones system, J. Chem. Phys. **118**, 7651 (2003).
[75] R. L. Davidchack and B. B. Laird, Crystal Structure and Interaction Dependence of the Crystal-Melt Interfacial Free Energy, Phys. Rev. Lett. **94**, 086102 (2005).
[76] R. Benjamin and J. Horbach, Crystal-liquid interfacial free energy via thermodynamic integration, J. Phys. Chem. **141**, 044715 (2014).
[77] F. Turci, T. Schilling, M. H. Yamani, and M. Oettel, Solid phase properties and crystallization in simple model systems, Eur. Phys. J.: Spec. Top. **223**, 421 (2014).
[78] Foiles, Development of an embedded-atom potential for a bcc metal: Vanadium, Phys. Rev. B **41**, 3316 (1990).
[79] R. A. Johnson and D. J. Oh, Analytic embedded atom method model for bcc metals, J. Mater. Res. **4**, 1195 (1989).
[80] J. Schmitz, J. Brillo, and I. Egry, Surface tension of liquid Al-Cu and wetting at the Cu/Sapphire solid-liquid interface, Eur. Phys. J.: Spec. Top. **223**, 469 (2014).
[81] Throughout this paper we employ the term hard spheres for both experimental and theoretical systems. Strictly speaking, there are no experimental HSs, just approximants, and much care has to be taken to ensure that the employed experimental systems are sufficiently close to computational HSs to serve as valid models. See the discussion in C. P. Royall, W. C. K. Poon, and E. R. Weeks, In search of colloidal hard spheres, Soft Matter **9**, 17 (2013).
[82] J. Hernández-Guzmán and E. R. Weeks, The equilibrium intrinsic crystal-liquid interface of colloids, Proc. Natl. Acad. Sci. USA **106**, 15198 (2009).
[83] R. B. Rogers and B. J. Ackerson, The measurement of solid-liquid interfacial energy in colloidal suspensions using grain boundary grooves, Philos. Mag. **91**, 682 (2011).
[84] V. Heinonen, A. Mijailovi, C. V. Achim, T. Ala-Nissila, R. E. Rozas, J. Horbach, and H. Löwen, Bcc crystal-fluid interfacial free energy in Yukawa systems, J. Chem. Phys. **138**, 044705 (2013).
[85] J. J. Hoyt, M. Asta, T. Haxhimali, A. Karma, R. E. Napolitano, R. Trivedi, B. B. Laird, and J. R. Morris, Crystal-Melt Interfaces and Solidification Morphologies in Metals and Alloys, MRS Bull. **29**, 935 (2004).
[86] R. E. Rozas and J. Horbach, Capillary wave analysis of rough solid-liquid interfaces in nickel, Europhys. Lett. **93**, 26006 (2011).
[87] S. Klein, D. Holland-Moritz, and D. M. Herlach, Crystal nucleation in undercooled liquid Zirconium, Phys. Rev. B **80**, 212202 (2009).
[88] S. Auer and D. Frenkel, Suppression of crystal nucleation in polydisperse colloids due to increase of the surface free energy, Nature (London) **413**, 711 (2001).
[89] U. Gasser, E. Weeks, A. Schofield, P. N. Pusey, and D. A. Weitz, Real-Space Imaging of Nucleation and Growth in Colloidal Crystallization, Science **292**, 258 (2001).
[90] S. Auer and D. Frenkel, Quantitative predictions for crystal nucleation rates for spherical colloids: a computational approach, Annu. Rev. Phys. Chem. **55**, 333 (2004).
[91] J. Bokeloh, R. E. Rozas, J. Horbach, and G. Wilde, Nucleation Barriers for the Liquid-To-Crystal Transition in Ni: Experiment and Simulation, Phys. Rev. Lett. **107**, 145701 (2011).
[92] F. Spaepen, A structural model for the solid-liquid interface in monatomic systems, Acta Metall. **23**, 729 (1975).
[93] F. Spaepen and R. B. Meyer, The surface tension in a structural model for the solid-liquid interface, Scr. Metall. **10**, 257 (1976).
[94] L. Gránásy and M. Tegze, Crystal-melt interfacial free energy of elements and alloys, Mater. Sci. Forum **77**, 243 (1991).
[95] H. J. Schöpe, G. Bryant and W. van Megen, Small changes in particle-size distribution dramatically delay and enhance nucleation in hard sphere colloidal suspensions, Phys. Rev. E **74**, 060401 (2006).
[96] M. Fasolo and P. Sollich, Equilibrium Phase Behavior of Polydisperse Hard Spheres, Phys. Rev. Lett. **91**, 068301 (2003).
[97] M. Fasolo and P. Sollich, Fractionation effects in phase equilibria of polydisperse hard-sphere colloids, Phys. Rev. E **70**, 041410 (2004).
[98] P. Sollich and N. B. Wilding, Crystalline Phases of Polydisperse Spheres, Phys. Rev. Lett. **104**, 118302 (2010).
[99] P. Sollich and N. B. Wilding, Polydispersity induced solid-solid phase transitions in model colloids, Soft Matter **7**, 4472 (2011).
[100] S. R. Ganagalla and S. N. Punnathanam, Free energy barriers for homogeneous crystal nucleation in a eutectic system of binary hard spheres, J. Chem. Phys. **138**, 174503 (2013).
[101] A. Kozina, P. Diaz-Leyva, E. Bartsch, and T. Palberg, Polymer-Enforced Crystallization of a Eutectic Binary Hard Sphere Mixture, Soft Matter **8**, 627 (2012).
[102] M. Fasolo and P. Sollich, Effects of colloid polydispersity on the phase behavior of colloid-polymer mixtures, J. Chem. Phys. **122**, 074904 (2005).
[103] M. N. van der Linden, A. van Blaaderen, and M. Dijkstra, Effect of size polydispersity on the crystal-fluid and crystal-glass transition in hard-core repulsive Yukawa systems, J. Chem. Phys. **138**, 114903 (2013).
[104] B. Cabane, J. Li, F. Artzner, R. Botet, C. Labbez, G. Bareigts, M. Sztucki, and L. Goehring, Hiding in plain

view: Colloidal self-assembly from polydisperse populations, arXiv:1511.02493v1.
[105] H. Lange, Comparative test of methods to determine particle size and particle size distribution in the submicron range, Part. Part. Syst. Charact. **12**, 148 (1995).
[106] M. Ballauff, SAXS and SANS studies of polymer colloids., Curr. Opn. Colloid Interface Sci. **6**, 132 (2001).
[107] S. Alexander, P. M. Chaikin, P. Grant, G. J. Morales, P. Pincus, and D. Hone, Charge renormalization, osmotic pressure, and bulk modulus of colloidal crystals: Theory, J. Chem. Phys. **80**, 5776 (1984).
[108] T. Gisler, S. F. Schulz, M. Borkovec, H. Sticher, P. Schurtenberger, B. D'Aguanno, and R. Klein, Understanding colloidal charge renormalization from surface chemistry: Experiment and theory, J. Chem. Phys. **101**, 9924 (1994).
[109] Y. Levin, Electrostatic correlations: from plasma to biology, Rep. Prog. Phys. **65**, 1577 (2002).
[110] L. Shapran, M. Medebach, P. Wette, H. J. Schöpe, T. Palberg, J. Horbach, T. Kreer, and A. Chaterji, Qualitative characterisation of effective interactions of charged spheres on different levels of organisation using Alexander's renormalised charge as reference, Colloids Surf., A **270–271**, 220 (2005).
[111] N. Garbow, M. Evers, T. Palberg, and T. Okubo, On the electrophoretic mobility of isolated colloidal spheres, J. Phys.: Condens. Matter **16**, 3835 (2004).
[112] P. Sollich, Predicting phase equilibria in polydisperse systems, J. Phys.: Condens. Matter **14**, R79 (2002).
[113] H. Löwen, J.-N. Roux, and J.-P. Hansen, Mapping of charge polydispersity onto size polydispersity in colloidal suspensions, J. Phys.: Condens. Matter **3**, 997 (1991).
[114] H. Löwen (private communication).
[115] N. Lorenz and T. Palberg, Melting and freezing lines for a mixture of charged colloidal spheres with spindle type phase diagram, J. Chem. Phys. **133**, 104501 (2010).
[116] N. Geerts, S. Jahn, and E. Eiser, Direct observation of size fractionation during colloidal crystallization, J. Phys.: Condens. Matter **22**, 104111 (2010).
[117] P. Wette, H. J. Schöpe, R. Biehl, and T. Palberg, Conductivity of deionised two-component colloidal suspensions, J. Chem. Phys. **114**, 7556 (2001).
[118] P. Wette, H. J. Schöpe, and T. Palberg, Experimental Determination of Effective Charges in Aqueous Suspensions of Colloidal Spheres, Colloids Surf., A **222**, 311 (2003).
[119] P. Wette, I. Klassen, D. Holland-Moritz, D. M. Herlach, H. J. Schöpe, N. Lorenz, H. Reiber, T. Palberg, and S. V. Roth, Complete description of re-entrant phase behavior in a charge variable colloidal model system, J. Chem. Phys. **132**, 131102 (2010).
[120] P. Wette and H. J. Schöpe, Consistence of the mean field description of charged colloidal crystal properties, Prog. Colloid Polym. Sci. **133**, 88 (2006).
[121] N. Lorenz, P. Wette, and T. Palberg (unpublished).
[122] P. Wette, Eigenschaftskorrelationen in kolloidalen Festkörpern und Fluiden aus optischen Experimenten, Ph.D. thesis, JGU Mainz, Mainz, 2005.
[123] N. J. Lorenz, H. J. Schöpe, H. Reiber, T. Palberg, P. Wette, I. Klassen, D. Holland-Moritz, D. Herlach, and T. Okubo, Phase behavior of deionized binary mixtures of charged colloidal spheres, J. Phys.: Condens. Matter **21**, 464116 (2009).
[124] S. Martin, G. Bryant, and W. van Megen, Crystallization kinetics of polydisperse colloidal hard spheres: Experimental evidence for local fractionation, Phys. Rev. E **67**, 061405 (2003).
[125] http://www.codata.info/resources/databases/key1.html
[126] A. Yazdi, A. Ivlev, S. Khrapak, H. Thomas, G. E. Morfill, H. Löwen, A. Wysocki, and M. Sperl, Glass-transition properties of Yukawa potentials: From charged point particles to hard spheres, Phys. Rev. E **89**, 063105 (2014).
[127] It is interesting to note that alternative descriptions of the particle interactions have been proposed and used in connection with the calculation of IFEs [see, e.g., M. Knott and I. J. Ford, Surface tensions and nucleation rates of phases of a charged colloidal suspension, Phys. Rev. E **65**, 061401 (2002)]. Such theories of like charge attraction were motivated by a number of experimental findings incompatible with standard DLVO theory in combination with strict equilibrium conditions and a homogeneous, gradient, and field-free solvent. Although some of the observations were traced back to either measuring artifacts or the presence of electrolyte gradients, others, like void formation, are not yet explained. Therefore, theories of like-charge attraction remain a controversial issue. For the presently investigated systems, however, the description of the interaction in terms of pairwise additive (hard-core) Yukawa potentials yields a consistent description of the phase behavior, the elasticity, and the diffusive dynamics and is therefore applied (see also Appendix B).
[128] D. Hessinger, M. Evers, and T. Palberg, Independent Ion Migration in Suspensions of Strongly Interacting Charged Colloidal Spheres, Phys. Rev. E **61**, 5493 (2000).
[129] M. Medebach, R. Chulia Jordán, H. Reiber, H.-J. Schöpe, R. Biehl, M. Evers, D. Hessinger, J. Olah, T. Palberg, E. Schönberger, and P. wette, Drude like conductivity in charged sphere colloidal crystals: density and temperature dependence, J. Chem. Phys. **123**, 104903 (2005).
[130] R. Klein, H. H. v. Grünberg, C. Bechinger, M. Brunner, and V. Lobashkin, Macroion shielding and state dependent pair potentials in colloidal suspensions, J. Phys.: Condens. Matter **14**, 7631 (2002).
[131] C. Russ, M. Brunner, C. Bechinger, and H. H. von Grünberg, Three-body forces at work: Three-body potentials derived from triplet correlations in colloidal suspensions, Europhys. Lett. **69**, 468 (2005).
[132] T. Kreer, J. Horbach, and A. Chatterji, Nonlinear effects in charge stabilized colloidal suspensions, Phys. Rev. E **74**, 021401 (2006).
[133] M. O. Robbins, K. Kremer, and G. S. Grest, Phase diagram and dynamics of Yukawa Systems, J. Chem. Phys. **88**, 3286 (1988).
[134] S. Hamaguchi, R. T. Farouki, and D. H. E. Dubin, Triple point of Yukawa systems, Phys. Rev. E **56**, 4671 (1997).
[135] F. Smallenburg, N. Boon, M. Kater, M. Dijkstra, and R. van Roij, Phase diagrams of colloidal spheres with a constant zeta-potential, J. Chem. Phys. **134**, 074505 (2011).
[136] A. P. Hynninen and M. Dijkstra, Phase diagrams of hard core repulsive Yukawa particles, Phys. Rev. E **68**, 021407 (2003).
[137] A. P. Hynninen, M. Dijkstra, and R. van Roij, Effect of triplett interactions on the phase diagram of suspensions of charged spheres, Phys. Rev. E **69**, 061407 (2004).

[138] A. P. Hynninen and M. Dijkstra, Melting line of charged colloids from primitive model simulations, J. Chem. Phys. **123**, 244902 (2005).
[139] A. P. Hynninen and M. Dijkstra, Phase diagram of hard-core repulsive Yukawa particles with a density-dependent truncation: a simple model for charged colloids, J. Phys.: Condens. Matter **15**, S3557 (2003).
[140] J. F. Millero, Thermodynamics of the carbon dioxide system in the oceans, Geochim. Cosmochim. Acta **59**, 661 (1995).
[141] Y. Monovoukas and A. P. Gast, A Study of Colloidal Crystal Morphology and Orientation via Polarizing Microscopy, Langmuir **7**, 460 (1991).
[142] A. Stipp, R. Biehl, Th. Preis, J. Liu, A. Barreira Fontecha, H. J. Schöpe, T. Palberg, Heterogeneous nucleation of colloidal melts under the influence of shearing fields, J. Phys.: Condens. Matter **16**, S3885 (2004).
[143] W. Luck, M. Klier, and H. Wesslau, Kristallisation übermolekularer Bausteine, Naturwissenschaften **50**, 485 (1963).
[144] A. Stipp and T. Palberg, Crystal Growth Kinetics in Binary Mixtures of Model Charged Sphere Colloids, Philos. Mag. Lett. **87**, 899 (2007).
[145] J. Liu and T. Palberg, Crystal growth and crystal morphology of charged colloidal binary mixtures, Progr. Colloid Polym. Sci. **123**, 222 (2004).
[146] H. J. Schöpe, The originally employed version of the fitting algorithm had a factor 2 missing (private communication).
[147] W. G. Hoover and F. H. Ree, Melting transition and communal entropy for hard spheres, J. Chem. Phys. **49**, 3609 (1968).
[148] W. B. Russel, On the dynamics of the disorder-order transition, Phase Transit. **21**, 127 (1990).
[149] J. Wagner, W. Härtl, and H. Walderhaug, Long time self diffusion in suspensions of highly charged colloids: a comparison between pulsed field gradient NMR and Brownian dynamics, J. Chem. Phys. **114**, 975 (2001).
[150] H. Löwen, T. Palberg, and R. Simon, A Dynamical Criterion for the Freezing of Brownian Particles, Phys. Rev. Lett. **70**, 1557 (1993).
[151] K. F. Kelton and A. F. Greer, *Nucleation in Condensed Matter Applications in Materials and Biology*, Pergamon Materials Series No. 15 (Pergamon, Amsterdam, 2010).
[152] J. L. Katz, Homogeneous nucleation theory and experiment: A survey, Pure Appl. Chem. **64**, 1661 (1992).
[153] A. Fladerer and R. Strey, Homogeneous nucleation and droplet growth in supersaturated argon vapor: The cryogenic nucleation pulse chamber, J. Chem. Phys. **124**, 164710 (2006).
[154] L. M. Feldmar, J. Wölk, and R. Strey, New measurements of argon and nitrogen nucleation in the cryogenic nucleation pulse chamber, AIP Conf. Proc. **1527**, 15 (2013).
[155] S. P. Das, *Statistical Physics of Liquids at Freezing and Beyond* (Cambridge University Press, Cambridge, UK, 2011).
[156] A. D. J. Haymet and D. W. Oxtoby, A molecular theory for the solid–liquid interface, J. Chem. Phys. **74**, 2559 (1981).
[157] D. W. Oxtoby and A. D. J. Haymet, A molecular theory of the solid–liquid interface II Study of bcc crystal–melt interfaces, J. Chem. Phys. **76**, 6262 (1982).
[158] D. Walton, Nucleation of Vapor Deposits, J. Chem. Phys. **37**, 2182 (1962).
[159] D. Kashchiev, Toward a better description of the nucleation rate of crystals and crystalline monolayers, J. Chem. Phys. **129**, 164701 (2008).
[160] A. Tröster, M. Oettel, B. Block, P. Virnau, and K. Binder, Numerical approaches to determine the interface tension of curved interfaces from free energy calculations, J. Chem. Phys. **136**, 064709 (2012).
[161] Ø. Wilhelmsen, D. Bedeaux, and D. Reguera, Tolman length and rigidity constants of the Lennard-Jones fluid, J. Chem. Phys. **142**, 064706 (2015).
[162] D. T. Wu, *Solid State Physics - Advances in Research and Applications*, Solid State Physics Vol. 50, edited by H. Ehrenreich and F. Spaepen (1997), pp. 37–187.
[163] N. M. Dixit and C. F. Zukoski, Nucleation kinetics and induction times during colloidal crystallisation: links between models and experiment, Phys. Rev. E **66**, 051602 (2002).
[164] D. M. Herlach, R. F. Cochrane, I. Egry, H. J. Fecht, and A. L. Greer, Containerless processing in the study of metallic melts and their solidification, Int. Mater. Rev. **38**, 273 (1993).
[165] D. Reguera and J. M. Rubí, Homogeneous nucleation in inhomogeneous media. I. Nucleation in a temperature gradient, J. Chem. Phys. **119**, 9877 (2003).
[166] D. Reguera and J. M. Rubí, Homogeneous nucleation in inhomogeneous media. II. Nucleation in a shear flow, J. Chem. Phys. **119**, 9888 (2003).
[167] P. G. Vekilov, Dense Liquid Precursor for the Nucleation of Ordered Solid Phases from Solution, Cryst. Growth Des. **4**, 671 (2004).
[168] D. Gebauer, M. Kellermeier, J. D. Gale, L. Bergström, and H. Cölfen, Pre-nucleation clusters as solute precursors in crystallisation, Chem. Soc. Rev. **43**, 2348 (2014).
[169] M. Schrader, P. Virnau, and K. Binder, Simulation of vapor-liquid coexistence in finite volumes: A method to compute the surface free energy of droplets, Phys. Rev. E **79**, 061104 (2009).